Emerin self-assembly and nucleoskeletal coupling regulate nuclear envelope mechanics against stress

Emerin oligomers resist nuclear stress

Anthony Fernandez[1], Markville Bautista[2], Liying Wu[1] and Fabien Pinaud[1,2,3*]

[1]Department of Biological Sciences, University of Southern California, 1050 Childs Way, Los Angeles, CA 90089, USA.

[2]Department of Chemistry, University of Southern California, 1050 Childs Way, Los Angeles, CA 90089, USA.

[3]Department of Physics and Astronomy, University of Southern California, 1050 Childs Way, Los Angeles, CA 90089, USA.

*Correspondence should be addressed to F.P. (pinaud@usc.edu)

Abstract

Emerin is an integral nuclear envelope protein participating in the maintenance of nuclear shape. When mutated or absent, emerin causes X-linked Emery-Dreifuss muscular dystrophy (EDMD). To define how emerin takes parts in molecular scaffolding at the nuclear envelope and helps protect the nucleus against mechanical stress, we established its nanoscale organization using single molecule tracking and super-resolution microscopy. We show that emerin monomers form localized oligomeric nanoclusters stabilized by both lamin A/C and SUN1 at the LINC complex. Interactions of emerin with nuclear actin and BAF additionally modulate its membrane mobility and its ability to oligomerize. In nuclei subjected to mechanical challenges, the mechanotransducing functions of emerin are coupled to changes in its oligomeric state, and the incremental self-assembly of emerin determines nuclear shape adaptation against forces. We also show that the abnormal nuclear envelope deformations induced by EDMD emerin mutants stem from an improper formation of lamin A/C and LINC complex-stabilized emerin oligomers. These findings place emerin at the center of the molecular processes that regulate nuclear shape remodeling in response to mechanical challenges.

Introduction

34

35   Emerin is an inner nuclear membrane (INM) protein that participates in the maintenance of the

36   nuclear architecture by interacting with the lamina and elements of the linker of the

37   nucleoskeleton and cytoskeleton (LINC) complex(Berk et al., 2013b; Kirby and Lammerding,

38   2018). Emerin also contributes to tethering chromatin at the nuclear envelope (NE) by binding

39   the DNA-bridging barrier-to-autointegration factor (BAF) and regulating the activity of

40   chromatin compaction modulators(Cui et al., 2015; Demmerle et al., 2012). Both the

41   nucleoskeleton and the compaction state of chromatin contribute to the mechanical responses of

42   nuclei and emerin is deemed a pivotal actor of mechanotransducing processes at the NE(Maurer

43   and Lammerding, 2019). When mutated or absent, emerin causes X-linked Emery-Dreifuss

44   muscular dystrophy (EDMD), a disease part of a larger of group of laminopathies associated

45   with structural perturbations of the NE and its underlying lamina(Emery and Dreifuss, 1966).

46   While emerin is ubiquitously expressed, mutations in the *EMD* gene primarily affect cells

47   exposed to extensive mechanical stress, such as skeletal and cardiac muscle cells. Emerin-null

48   muscle tissues display deformed and disorganized nuclei, impaired myogenesis and improper

49   muscle fiber formation, which participate in the muscle wasting and cardiac disease phenotypes

50   of EDMD(Fidzianska and Hausmanowa-Petrusewicz, 2003). In non-muscle cells, loss of emerin

51   also induces altered NE elasticity and increased nuclear fragility(Rowat et al., 2006), impaired

52   expression of mechanosensitive genes and enhanced apoptosis after mechanical

53   strain(Lammerding et al., 2005). EDMD phenotypes might stem from both an altered structural

54   integrity of the NE and modified gene expression profiles.

55   The structure of emerin and its binding to various partners have been extensively

56   characterized(Berk et al., 2013b). Emerin is 254 amino acids (aa) long, with a N-terminal

57   globular LAP2-emerin-MAN1 domain (LEM, aa:1-45), followed by a long intrinsically

58   disordered region (IDR, aa:46-222) and a C-terminal transmembrane domain (aa:223-234) that

59   allows anchoring to the NE. Prominent binding partners of emerin include lamin A/C and lamin

60   B(Clements et al., 2000; Sakaki et al., 2001), actin(Fairley et al., 1999), BAF(Lee et al., 2001),

61   nesprins and SUN proteins from the LINC complex(Haque et al., 2010; Mislow et al., 2002) and

62   other factors(Berk et al., 2013b). While binding of emerin to BAF takes place via the LEM

63   domain, interactions with other partners and emerin self-association are mediated by the

64   IDR(Berk et al., 2014; Herrada et al., 2015). Emerin can indeed oligomerize via IDR segments

2

65   that serve as LEM binding and self-assembly sites between emerin monomers, and, in vitro,

66   emerin self-association into filamentous structures impacts binding to lamin A/C and BAF(Berk

67   et al., 2014; Samson et al., 2017). Post-translational modifications of emerin also influence its

68   oligomerization and its interactions with binding partners(Berk et al., 2013a; Roberts et al.,

69   2006). In isolated nuclei, phosphorylation of emerin residues Y74 and Y95 are required for lamin

70   A/C recruitment to the LINC complex and NE stiffening in response to mechanical

71   loads(Guilluy et al., 2014). Additional post-translational modifications regulate the affinity of the

72   LEM domain to BAF(Berk et al., 2013a) and binding to actin(Hirano et al., 2005). How emerin

73   organizes at the NE and participates in protecting the nucleus against mechanical strains remains

74   unclear.

75   EDMD often involves frame-shift deletions and nonsense mutations that effectively ablates

76   emerin expression in cells. Yet, a few sets of point mutations and deletions, including Δ95-99,

77   Q133H and P183H/T, also cause EDMD despite the localization of these mutated emerin at the

78   NE and normal cellular expression levels(Fairley et al., 1999; Holt et al., 2001). These mutants

79   display altered self-association and binding to nucleoskeletal proteins in vitro(Berk et al., 2013b;

80   Herrada et al., 2015) and possible changes in their molecular organizations at the NE might

81   explain why they induce EDMD.

82   Here, we used super-resolution imaging by direct stochastic optical reconstruction microscopy

83   (dSTORM)(van de Linde et al., 2011) and single particle tracking by photoactivated localization

84   microscopy (sptPALM)(Subach et al., 2010) to investigate the nanoscale organization of wild-

85   type and mutant emerin in cells. By modulating the mechanical landscape of nuclei using cell

86   micropatterning techniques(Fernandez et al., 2017), we also studied how emerin participates in

87   NE mechanotransduction processes during stress. We show that emerin oligomerization and its

88   differential interactions with key structural partners at the NE is central to nuclear shape

89   adaptation against mechanical challenges.

90

91

92   ## Results

93   **Emerin displays distinct diffusive behaviors at the nuclear envelope**

94   To study the NE dynamics of wild-type and dystrophy causing mutations of emerin, PA-

95   TagRFP-emerin fusions were expressed in emerin-null human dermal fibroblasts (HDF) from an

96   EDMD patient ($EMD^{-/y}$). PA-TagRFP-emerin expression led to its expected localization at the

97   NE, as observed for endogenous emerin in HDF from a healthy individual ($EMD^{+/y}$) (Fig. 1A).

98   Upon re-expression of wild-type emerin fusions in $EMD^{-/y}$ HDF, nuclear deformations against

99   mechanical stress recovered to levels similar to wild-type $EMD^{+/y}$ HDF(Bautista et al., 2019).

100   For sptPALM, individual PA-TagRFP-emerin were imaged using highly inclined and laminated

101   optical sheet excitation at the ventral NE(Tokunaga et al., 2008). Diffusion tracks were generated

102   from localized emerin appearances (Fig. 1B; Movie S1) and analyses were performed using the

103   probability distribution of square displacements (PDSD)(Schutz et al., 1997) to separate unique

104   diffusive behaviors (Fig. 1C).

105   We observed that wild-type emerin exhibits four distinct diffusive behaviors with diffusion

106   coefficients D_1: $2.21 \times 10^{-1} \pm 4.9 \times 10^{-2}$ $\mu m^2 s^{-1}$, a value similar to that reported for ER membrane

107   diffusion(Ostlund et al., 1999), D_2: $1.48 \times 10^{-2} \pm 1.5 \times 10^{-3}$ $\mu m^2 s^{-1}$, D_3: $1.73 \times 10^{-3} \pm 1.1 \times 10^{-4}$ $\mu m^2 s^{-1}$,

108   and D_4: $2.6 \times 10^{-4} \pm 1 \times 10^{-5}$ $\mu m^2 s^{-1}$ (Fig. 1D; Table S1). The ER population D_1 makes up 1% of the

109   detected behaviors, while population D_2 represents 9%, a small emerin fraction comparable to

110   that expected at the outer nuclear membrane (ONM)(Salpingidou et al., 2007). The two slowest

111   populations D_3 and D_4 collectively represent 90% of emerin diffusive behaviors. Based on their

112   individual diffusion coefficient, we grouped emerin trajectories into four diffusion ranges and

113   plotted them as maps. In trajectory maps, the fastest emerin population D_1 primarily distributes

114   in the vicinity of the NE, consistent with diffusion in the ER membrane, while the three slower

115   populations D_{2-4} are enriched at the NE (Fig. 1E). Compared to measurements by fluorescence

116   recovery after photobleaching, where only two diffusive behaviors of emerin were detected (Fig.

117   S1), sptPALM reveals that emerin has four distinct types of diffusions.

118

Emerin organizes as slowly diffusing monomers or oligomers at the inner nuclear membrane

121   While emerin primarily localizes at the INM, it is often detected at the ONM, where it does not

122   interact with the nuclear lamina. To assess if diffusing population D_2 corresponds to ONM-

123   associated emerin, sptPALM was done after lamin A/C depletion by siRNA (Fig. S2).

124   Downregulating the expression of lamin A/C did not affect emerin populations D_1 and D_2 (*p* not

125   significant, Fig. 2A) but the mobility of populations D_3 (40%) and D_4 (50%) increased (*p*<0.01,

126   Fig. 2A; Table S1), consistent with their localization at the INM and with population D_2

127   diffusing at the ONM. Commensurate with the majority of emerin being distributed as two

128   distinct INM pools, nuclear actin depletion by downregulating the expression of the actin nuclear

129   import factor importin-9(Dopie et al., 2012) (IPO9, Fig. S2-S3) also resulted in the increased

130   mobility of populations D_3 and D_4, although faster emerin diffusion at the ONM was also

131   observed, for equivocal reasons (Fig. 2A; Table S1). The 9% fraction of emerin diffusing at the

132   ONM agreed well with quantitative immunostaining measurements indicating that 13±6% of the

133   emerin pool localizes at the ONM in $EMD^{+/y}$ HDF (Fig. S4).

134   Emerin can self-assemble in vitro, which could induce its slow INM mobility if emerin

135   oligomers are tethered by the nucleoskeleton. To determine if diffusing populations D_3 or D_4

136   correspond to emerin monomers or oligomers, we co-expressed wild-type emerin fused to self-

137   complementary split-GFP fragments (Fig. 2B), induced the formation of complemented emerin-

138   GFP-emerin species and tracked their mobility by complementation activated light microscopy

139   (CALM)(Pinaud and Dahan, 2011). We found that emerin-GFP-emerin species localize almost

140   exclusively at the NE (Fig. 2C; Movie S2), with 90% diffusing like population D_4 (*p* not

141   significant, Fig. 2D) and 10% diffusing like the ONM population D_2 (*p* not significant, Fig. 2D).

142   No fluorescent species with mobility matching those of the ER population D_1 or the INM

143   population D_3 were detected. Emerin-GFP-emerin trajectories often spatially overlap, suggesting

144   that emerin forms multimers rather than strictly dimers at the INM (Fig. 2C). This indicates that

145   population D_3 detected by sptPALM but not by CALM represents emerin monomers, while the

146   slowest population D_4 represents INM emerin oligomers, as subsequently confirmed by super-

147   resolution imaging. The detection of a few emerin-GFP-emerin species at the ONM is likely due

148   to split-GFP-induced emerin dimers that cannot translocate through peripheral nuclear pore

149   channels and do not access the INM.

150

151   **BAF binding modulates the mobility of both emerin monomers and oligomers distributed**

152   **across the inner nuclear membrane.**

153   BAF binds the LEM domain of emerin with high affinity and could participate in the slow INM

154   diffusion of emerin via its additional interactions with lamin A/C(Samson et al., 2018) and

155   chromatin(Burger et al., 2020). To study how binding of emerin to BAF influences its mobility,

156   endogenous BAF was depleted by siRNA (Fig. S2) and replaced by the expression of BAF^{L58R}, a

5

157   mutant that does not bind LEM domains but binds lamin A/C and chromatin(Samwer et al.,

158   2017). When unable to bind BAF^{L58R}, emerin monomers and oligomers diffuse significantly

159   faster at the INM, with lateral mobilities higher than for lamin A/C or IPO9 knockdown ($p<0.01$,

160   Fig. 2A; Table S1). While emerin diffusion at the ER is undisturbed, its ONM mobility increases

161   ($p<0.01$, Fig. 2A), suggesting that cytoplasmic BAF also interacts with emerin at the ONM. BAF

162   being highly mobile in the nucleus(Shimi et al., 2004), the comparatively slow mobility of BAF-

163   bound emerin likely stems from the formation of ternary complexes with lamin A/C or

164   chromatin. As knockdown of endogenous BAF and expression of BAF^{L58R} did not alter the

165   expression of lamin A/C nor its nuclear localization (Fig. S2), the stronger influence of BAF^{L58R}

166   on emerin dynamics as compared to lamin A/C depletion indicates that BAF not only modulates

167   the mobility of emerin via ternary binding to lamin A/C, but also via additional interactions with

168   other nuclear components, potentially chromatin.

169   The global influence of BAF and the nucleoskeleton on the mobility of emerin was also captured

170   in diffusion maps built by spatial rendering of diffusion coefficients at the position of each

171   tracked PA-tagRFP-emerin (Fig. 2E). In those map, slow diffusion domains attributed to emerin

172   oligomers are distributed throughout the NE and are surrounded by areas where the mobility of

173   emerin is faster, as expected for monomers (Fig. 2E). This indicates a membrane-wide, yet

174   locally structured distribution of emerin, with monomers surrounding oligomer domains,

175   consistent with emerin monomer/oligomer exchanges in distinct INM areas. Together, these

176   results show that emerin diffuses rapidly at the ER membrane on its way to the juxtaposed ONM,

177   where its diffusion is slower, in part by interaction with cytoplasmic BAF. Once at the INM, the

178   mobility of emerin is further reduced, with monomers and oligomers interacting with nuclear

179   BAF and the nucleoskeleton, consistent with a combined BAF-induced and lamina-induced

180   retention of emerin at the INM.

181

182   Emerin forms discrete oligomeric nanodomains surrounded by monomers

183   We then probed the organization of emerin in greater detail using super-resolution microscopy.

184   Wild-type emerin fused to a SNAP-tag was expressed in $EMD^{-/y}$ HDF and imaged at the ventral

185   NE by dSTORM with benzylguanine-AlexaFluor647 (Fig. 3A). Emerin neighborhood density

186   functions (NDF) built from localized emerin positions were compared to MonteCarlo

187   simulations of completely random distributions and fitted to measure molecular densities and

188 length scales of significant clustering. We found that wild-type emerin is not distributed

189 randomly at the NE, as it displays density distributions significantly higher than expected for a

190 completely random organization (Fig. 3B). NDF were best fitted with a two-exponential decay

191 model, indicating that emerin organizes into two distinct clustering states across the NE. The first

192 clusters have typical sizes of 22±11 nm and molecular densities of emerin 8.2±0.2 fold higher

193 than expected for a random distribution (Fig. 3C; Table S2). The second clusters are significantly

194 larger with typical sizes of 236±30 nm and emerin densities slightly above the expected value of

195 1 for complete randomness (1.3±0.1 fold, Fig. 3C). In local cluster maps, emerin forms small

196 high-density clusters bordered by larger NE areas with emerin densities close to random (Fig.

197 3D). Those distributions are similar to sptPALM diffusion maps and corroborate that emerin

198 organizes into discrete oligomers surrounded by dispersed emerin monomers across the INM. A

199 similar organization of emerin was observed at the dorsal NE (Fig. S5). While it is intriguing that

200 emerin monomers appear slightly clustered, their completely random distribution is not expected

201 because they do not populate membrane-less areas of the NE, such as nuclear pores.

202

203 Emerin oligomers are stabilized by lamin A/C and SUN1 at LINC complexes and are

204 modulated by nuclear actin and BAF

205 We then determined how lamin A/C, nuclear actin, BAF and SUN1 from the LINC complex

206 participate in the spatial organization of emerin at the INM. Wild-type emerin was imaged by

207 dSTORM after siRNA knockdown of lamin A/C, IPO9, SUN1, or replacement of endogenous

208 BAF with BAF^{L58R}. After lamin A/C depletion, the molecular density of emerin is reduced (Fig.

209 3B) and emerin distributes into 35±17 nm nanodomains with densities close to random (1.2±0.1

210 fold, Fig. 3C; Table S2) and into large 950±173 nm monomer domains with densities just above

211 random (1.1±0.1 fold, Fig. 3C). Compared to controls, emerin monomers are dispersed over

212 larger areas and oligomers nearly vanish, as seen in emerin cluster maps of lamin A/C-depleted

213 nuclei (Fig. 3E). The spatial distribution of emerin and oligomerization returned to near normal

214 levels upon exogenous expression of a siRNA-resistant lamin A/C (Fig. 3C and S6), but

215 overexpression induced a loss of emerin oligomers (Fig. S6), indicating that balanced levels of

216 lamin A/C are essential to promote emerin self-assemblies. Although lamin A/C depletion

217 indirectly led to decreased nuclear actin levels (Fig. S2), emerin oligomers were not as severely

218 disrupted when nuclear actin was specifically depleted, as shown next. These results indicate that

219   lamin A/C plays a central role for the formation and the stabilization of emerin oligomers and

220   additionally influences the spatial distribution of emerin monomers at the INM.

221   When nuclear actin is depleted after IPO9 knockdown, emerin forms oligomers having reduced

222   molecular densities of 3.6 ± 0.1 fold above random and sizes of 65 ± 13 nm (Fig. 3C; Table S2).

223   Emerin monomers are dispersed over 382 ± 81 nm domains, larger than in untreated cells (236 ± 30

224   nm, Fig. 3C), but not as large as for lamin A/C depletion (950 ± 173 nm, Fig. 3C). Thus, despite

225   reduced nuclear actin levels, emerin still oligomerizes but redistributes over broader INM

226   domains. Conversely, nuclear accumulation of actin by siRNA of exportin 6 (XPO6, Fig. S3) did

227   not affect the organization of emerin monomers, but oligomer densities decreased to 1.5 ± 0.1 fold

228   above random in 49 ± 16 nm nanodomains (Fig. S7), suggesting that excess nuclear actin impedes

229   the formation of dense emerin oligomers. Thus, together with lamin A/C, nuclear actin

230   contributes to the spatial organization of emerin at the INM and participates in the maintenance

231   of emerin oligomers.

232   When endogenous BAF is replaced by BAF^{L58R}, emerin oligomers are still formed but with

233   reduced molecular densities of 2.0 ± 0.1 fold above random and larger sizes of 85 ± 19 nm

234   compared to controls (Fig. 3C; Table S2). The inability to bind BAF also induces a redistribution

235   of emerin monomers over large INM domains with typical sizes of 718 ± 250 nm (Fig. 3C).

236   Consistent with our diffusion results, emerin binding to BAF modulates the organization of both

237   oligomeric and monomeric emerin and strongly influences the spatial distribution of emerin

238   monomers at the INM.

239   When SUN1 is depleted to destabilize LINC complexes (Fig. S2), the formation of emerin

240   oligomers is reduced to levels equivalent to lamin A/C depletion. Emerin distributes over 75 ± 41

241   nm nanodomains with molecular densities decreased to 1.2 ± 0.1 fold above random (Fig. 3F;

242   Table S2), and over NE areas with sizes of 268 ± 110 nm, similar to the spatial distribution of

243   emerin monomers in untreated cells (Fig. 3F). This indicates that reduced SUN1 expression

244   levels primarily influence the formation of emerin oligomers at the INM. In cluster maps,

245   depletion of SUN1 effectively results in a largely random distribution of emerin and, like for

246   lamin A/C depletion, few emerin clusters are visible (Figure 3G). This loss of emerin oligomers

247   was partially rescued upon expression of an exogenous and siRNA-resistant EGFP-SUN1 (Fig.

248   3F and Fig. S6), but overexpression induced a mis-localization of both EGFP-SUN1 and emerin

249   from the NE (Fig.S6) and a concomitant reduction in emerin oligomerization (Fig. S6),

250 indicating that, as for lamin A/C, a balanced cellular expression of SUN1 is required for the self-
251 assembly of emerin at the INM. While SUN1 interacts with lamin A(Crisp et al., 2006; Haque et
252 al., 2006), the expression and NE localization of lamin A/C was not disrupted by SUN1
253 knockdown and, reciprocally, lamin A/C depletion did not modify the expression of SUN1 nor
254 its distribution at the NE (Fig. S2). Thus, together with lamin A/C, a regulated expression of
255 SUN1 is required for the formation of emerin oligomers and their localized distribution at the
256 INM. SUN1, itself, was shown to self-assemble into nearly immobile platforms that could serve
257 as sites for macromolecular assemblies at LINC complexes(Hennen et al., 2018; Lu et al., 2008).
258 To assess if emerin locally oligomerizes at LINC complexes, we expressed a dominant negative
259 KASH domain of nesprin-1α (mCherry-DN-KASH)(Lombardi et al., 2011), which disrupts
260 LINC complexes by binding to SUN proteins and impeding their interaction with endogenous
261 KASH-domain proteins at the NE. In cells expressing mCherry-DN-KASH, emerin oligomers
262 were disrupted at levels equivalent to those of SUN1 siRNA (Fig. 3C; Table S2), indicating that
263 the oligomerization of emerin requires a functional coupling of the nucleoskeleton and the
264 cytoskeleton via SUN1/nesprin interactions at LINC complexes.
265 Together, these results show that emerin monomers are distributed across the INM where their
266 distribution is modulated by direct binding to BAF and additional spatial constrains imposed by
267 lamin A/C and nuclear actin. Emerin also self-assembles into discrete and small oligomeric
268 nanodomains that are structurally co-stabilized at the LINC complex by lamin A/C and SUN1
269 and are maintained, to a lesser extent, by BAF and nuclear actin.

270

271 **Increased diffusion and oligomerization of emerin upon nuclear adaptation to mechanical**
272 **stress**
273 We then studied how the mobility of emerin and its organization change in nuclei subjected to
274 increasing mechanical stress. SptPALM and super-resolution imaging of wild-type emerin were
275 done in $EMD^{-/y}$ HDF grown on increasingly narrow rectangular micropatterns with widths of 15-
276 5 µm to impose steady-state mechanical stress to the nucleus (Fig. 4A-B) and increase
277 mechanical loads at LINC complexes(Arsenovic et al., 2016). First, we verified that changes in
278 nuclear shape index (NSI) on these micropatterns reflect the mechanical adaptation of nuclei
279 against forces by depleting lamin A/C or nuclear actin, two key nucleoskeletal proteins involved

280   in maintaining nuclear shape. In non-patterned cells, nuclei are less circular after lamin A/C or

281   nuclear actin depletion compared to controls ($p<0.01$, Fig. 4C). These effects are amplified on

282   micropatterns where nuclei become increasingly deformed as patterns get narrower ($p<0.01$, Fig.

283   4C), indicating that cell micropatterning elicits increased nuclear stress and effectively induces

284   mechanical responses that implicate the nucleoskeleton.

285   When we tracked wild-type PA-tag-RFP-emerin on deformed nuclei in 15 µm and 10 µm

286   patterns (Movie S3), we found that its ER mobility is unchanged compared to non-patterned cells

287   (p not significant, Fig. 4D; Table S1), while its diffusion at the ONM is faster ($p<0.01$, Fig. 4D).

288   At the INM, emerin monomers also diffuse significantly faster ($p<0.01$, Fig. 4D) and the

289   mobility of oligomers increases, albeit short of statistical significance for 15 µm patterns (p not

290   significant and $p<0.01$, Fig. 4D). Interestingly, there was no significant difference in the mobility

291   of all four ER, ONM and INM emerin populations in both types of micropatterns compared to

292   nuclear actin depletion (p not significant, Fig. S8), suggesting that nuclear shape adaptation to

293   mechanical cues entails modified interactions of emerin with nuclear actin, notably for

294   monomers.

295   Spatial distribution analyses further indicate that, as the NSI decreases, emerin monomers

296   disperse over increasingly large INM domains with sizes of 382 ± 62 nm and 460 ± 136 nm,

297   compared to 236 ± 30 nm for non-stressed nuclei (Fig. 4E). Concurrently, oligomer densities drop

298   from 8.2 ± 0.2 fold to 3.6 ± 0.1 fold above random in 15 µm patterns, before increasing to 4.6 ± 0.1

299   fold above random in 10 µm patterns (Fig. 4E). Remarkably, oligomeric nanodomains become

300   larger during nuclear stress and their size expands from 22 ± 11 nm to 60 ± 13 nm in both

301   micropatterns (Fig. 4E). When considering this wider spatial distribution, the relative

302   oligomerization of emerin compared to non-deformed nuclei increases by 3.4 fold and by 4.1

303   fold as the nucleus adapts to incremental mechanical stress (Fig. 4F). This shows that nuclear

304   shape adaptation to forces is associated with a gradual change in the oligomerization potential of

305   emerin at the INM. This increased self-assembly of emerin over larger nanodomains is

306   accompanied by a faster lateral mobility of emerin and is triggered by nucleoskeletal re-

307   arrangements. Indeed, the stress-induced spatial reorganizations of emerin in micropatterns,

308   including oligomer densities and emerin domain sizes, are analogous to those seen when nuclear

309   actin is depleted in non-patterned cells (Fig. S8; Table S2). Consistent with the contribution of

310   nuclear actin to changes in nuclear volume(Baarlink et al., 2017), these observations suggest that

10

311   nuclear shape deformation involves a disengagement of nuclear actin from the nucleoskeleton

312   that results in faster emerin diffusion and increased oligomerization. Increased lateral mobilities

313   of emerin at the INM could indeed facilitate molecular collisions between monomers and the

314   formation of oligomers stabilized by lamin A/C and SUN1 at LINC complexes. These results

315   indicate that the mechanotransducing functions of emerin are coupled to changes in its

316   oligomeric state along the INM and are modulated by emerin interactions with nucleoskeletal

317   partners, including nuclear actin, to ensure appropriate nuclear deformation and response to

318   mechanical challenges.

319

320   **Emerin mutants induce abnormal nuclear deformation against mechanical stress**

321   To further establish the significance of emerin oligomerization for nuclear adaptation to

322   mechanical stress, we then compared the organization of wild-type emerin with that of mutated

323   forms of emerin known to induce EDMD. We studied how mutation Q133H, deletion Δ95-99,

324   and mutation P183H (Fig. 5A) affect the diffusion and the nanoscale distribution of emerin at the

325   NE. First, we verified that these mutated emerin effectively induce defective mechanical

326   responses of nuclei when expressed in $EMD^{-/y}$ HDF by comparing changes in NSI after random

327   cell plating or plating on increasingly narrow micropatterns (Fig. 5B-C). In randomly plated

328   cells, the expression of mutated emerin results in slightly less circular nuclei compared to wild-

329   type emerin (Fig. 5B). With increasing mechanical stress, cells expressing emerin mutants

330   display significantly higher NSI than wild-type (Fig. 5B), indicative of a failure to correctly

331   modify the shape of the nucleus in response to forces. These deficient changes in nuclear shape

332   are accompanied by a mispositioning of the nucleus relative to the cell major axis, nucleus

333   crumpling, abnormal organization of the actin cytoskeleton and failure of cells to properly fit

334   within micropatterns, specifically in cell areas adjacent to the misshaped nucleus (Fig. 5C). It

335   indicates that expression of mutated emerin in $EMD^{-/y}$ HDF effectively impedes nuclear

336   adaptation to mechanical stress.

337

338   **Emerin mutants display defective oligomerization at the inner nuclear membrane**

339   **Q133H mutation.** We then characterized the NE dynamics of each mutated emerin and their

340   respective nanoscale organization, starting with Q133H emerin. We found that the lateral

11

341 mobility of Q133H PA-TagRFP-emerin is similar to that of wild-type emerin at the ER and the

342 ONM (p not significant, Fig. 6A; Table S1), but that both Q133H monomers and oligomers

343 diffuse significantly faster at the INM ($p<0.01$ and $p<0.05$, Fig. 6A). Previous in vitro studies

344 indicated that the Q133H mutation disrupts emerin binding to actin(Holaska et al., 2004) but

345 does not impede interactions with lamin A/C(Holt et al., 2001), SUN1(Haque et al., 2010) or

346 BAF(Bengtsson and Wilson, 2004). The increased INM diffusion of Q133H, therefore suggests

347 that it does not bind nuclear actin. Interestingly, this faster INM diffusion of Q133H resembles

348 the increased mobility of wild-type emerin when nuclear actin is depleted (Fig. 2A), which

349 further underlines that nucleoskeletal actin modulates the diffusion of emerin monomers and

350 oligomers. This is consistent with previous observations that emerin expression influences the

351 mobility of nuclear actin(Ho et al., 2013) and indicative of a reciprocal effect of emerin/nuclear

352 actin interactions on their respective mobility. The diffusion of Q133H at the INM is also similar

353 to that of wild-type emerin under mechanical stress, in both 15 µm and 10 µm wide

354 micropatterns (p not significant, Fig. S8), which supports a mechanism where nuclear

355 deformations involve a dissociation of emerin from nuclear actin that leads to faster emerin

356 diffusion at the INM.

357 Although, it was reported that Q133H has a reduced capacity to self-assemble in vitro(Herrada et

358 al., 2015), its spatial distribution and cluster maps show that it organizes into monomers and

359 oligomers across the INM (Fig. 6B-C). Like wild-type emerin, Q133H monomers are distributed

360 in 213±62 nm membrane domains (Fig. 6B), an indication that the inability to bind nuclear actin

361 increases the mobility of Q133H monomers but does not affect their overall spatial distribution at

362 the INM. Q133H also maintain the ability to self-assemble at the INM where it forms oligomeric

363 clusters having sizes of 19±12 nm, comparable to the 22±11 nm size of wild-type emerin

364 oligomers, but with molecular densities 12.2±0.2 fold above random (Fig. 6B-C; Table S2). This

365 50% increase in oligomerization compared to wild-type indicates that deficient binding of

366 Q133H to nucleoskeletal actin leads to a disproportionate self-assembly of emerin into

367 oligomeric nanodomains. It also implies that direct binding to nuclear actin normally reduces the

368 oligomerization potential of wild-type emerin, consistent with our observation that excessive

369 nuclear accumulation of actin impedes the formation of emerin oligomers at the INM (Fig. S7).

370

371 **Δ95-99 mutation.** When we performed similar studies with Δ95-99 emerin, we found that
372 diffusions at the ER membrane and the ONM are unchanged compared to wild-type emerin (p
373 not significant, Fig. 6D; Table S1), but that lateral mobilities at the INM are significantly
374 reduced ($p<0.05$ and $p<0.01$, Fig. 6D), with the slowest Δ95-99 emerin population being
375 essentially immobile. This suggests that Δ95-99 interacts more strongly or more frequently than
376 wild-type emerin with some of its binding partners on the nucleoplasmic side of the NE.
377 Previous biochemical studies have shown that the Δ95-99 deletion disrupts emerin interactions
378 with most of its binding partners, including lamin A/C and actin, but not BAF(Berk et al.,
379 2013b). As BAF binding strongly influences the mobility of wild-type emerin (Fig. 2A), the
380 reduced diffusion of Δ95-99 at the INM could stem from repetitive interactions with BAF, as
381 recently proposed(Samson et al., 2017). To destabilize these interactions, we attempted to track
382 Δ95-99 in *EMD*$^{-/y}$ HDF knocked down for endogenous BAF and expressing BAF^{L58R}. Co-
383 expression of both Δ95-99 and BAF^{L58R}, however, proved toxic to cells, indicating that
384 interactions between Δ95-99 emerin and BAF are important to maintain cell viability.

385 In addition to its slow mobility, Δ95-99 displays defective oligomerization at the INM. Δ95-99 is
386 distributed randomly over large, 420±51 nm NE domains and in smaller, 48±14 nm
387 nanodomains where the molecular density of 1.3±0.1 fold above random is greatly reduced
388 compared to wild-type emerin oligomers (Fig. 6E; Table S2). Effectively, Δ95-99 forms less
389 dense and fewer oligomerization nanodomains in cluster maps (Fig. 6F). Thus, Δ95-99 does not
390 efficiently oligomerize at the INM, consistent with its impaired self-assembly in vitro and reports
391 that the deletion lowers emerin/emerin proximity(Herrada et al., 2015). Interestingly, despite an
392 intact lamina and the preserved ability of Δ95-99 to bind SUN1(Haque et al., 2010), the
393 molecular densities and cluster maps of Δ95-99 are similar to those of wild-type emerin when the
394 expression of lamin A/C is reduced or when SUN1 LlNC complexes are disrupted (Fig. 3C-D).
395 This reduced oligomerization of Δ95-99 to levels seen after lamin A/C depletion implies that
396 direct binding to lamin A/C is required to stabilize emerin oligomers at SUN1 LINC complexes.
397 Such a stabilizing role of lamin A/C is consistent with prior proximity ligation assays where
398 Δ95-99 was found less close to lamin A/C than wild-type emerin(Herrada et al., 2015) and
399 studies showing that the deletion abolishes direct lamin A/C binding to emerin(Lee et al., 2001).
400 Together, these results show that Δ95-99 primarily distributes at random across the INM due to
401 its reduced self-assembly, its inability to directly bind lamin A/C and its slow mobility.

402

P183H mutation. Like for the other emerin mutants, the diffusion of P183H emerin at the ER membrane and the ONM is unchanged compared to wild-type emerin (*p* not significant, Fig. 6G; Table S1). However, its INM mobility is reduced for the populations attributed to monomers and oligomers (*p*<0.05 and *p*<0.01, Fig. 6G), with the slowest P183H population being immobile. This slow diffusion resembles that observed for Δ95-99 and again implies that P183H interacts more frequently than wild-type emerin with some of its nucleoplasmic binding partners. In vitro, P183H binds SUN1(Haque et al., 2010), BAF and actin(Berk et al., 2013b) and displays enhanced binding to lamin A/C compared to wild-type emerin(Lee et al., 2001). Its reduced INM mobility might therefore be linked to an increased binding frequency to BAF, like for Δ95-99, or to its enhanced binding to lamin A/C. The slow diffusion of P183H could also be due to the formation of dimers as suggested based on its strong propensity to self-assemble in vitro(Herrada et al., 2015) and observations that residue P183 is positioned in the 168-186 emerin region required to limit emerin-emerin association(Berk et al., 2014). To determine if P183H forms dimers, we performed tracking by CALM after co-expression of P183H fused to split-GFP fragments. Three populations of P183H-GFP-P183H emerin species were detected: a 2% population with a mobility slightly slower than P183H at the ER membrane (*p*<0.05, Fig. 6G), a larger 39% population with a mobility comparable to the ONM behavior of P183H (*p* not significant, Fig. 6G), and a dominant 59% population with a lateral diffusion similar to the INM population initially attributed to P183H monomers by sptPALM (*p* not significant, Fig. 6G; Table S1). Surprisingly, no fluorescent species with diffusion coefficient matching that of the immobile P183H oligomers are detected (Fig. 6G). The high frequency detection of complemented P183H-GFP-P183H emerin species at both the ER membrane and the ONM indicates that P183H is indeed more prone to form dimers than wild-type emerin before reaching the INM. This apparent biased monomer:dimer equilibrium towards dimers is maintained at the INM where it precludes an efficient association of P183H into oligomer domains, in particular if dimers are stabilized by irreversible assembly of the split-GFP fragments. This indicates that P183H has a strong propensity to form dimers that could impact oligomerization at the INM. Consistent with these observations, the dimerization of P183H leads to a significantly reduced oligomerization at the INM. P183H monomers/dimers are distributed in domains with typical sizes of 321±29 nm and molecular densities of 1.3±0.1 fold above random (Fig. 6H; Table S2).

433 Smaller, 35±12 nm nanodomains are also observed, but their molecular density is reduced to
434 2.2±0.1 compared to wild-type oligomers (Fig. 6H). Indeed, while P183H can still bind lamin
435 A/C and SUN1, it forms oligomeric domains having lower molecular density than wild-type
436 emerin in cluster maps (Fig. 6J), indicating that the dimerization of P183H hinders further self-
437 association into dense oligomers at the INM.

438

439

440 **Abnormal reorganization of Δ95-99 emerin in response to mechanical stress**

441 To characterize the importance of emerin oligomerization for nuclear deformation and responses
442 to mechanical stress, we also studied the nanoscale reorganization of Δ95-99 in micropatterned
443 cells. For deformed nuclei in 15 µm patterns, Δ95-99 monomers are dispersed over large,
444 810±215 nm INM domains, almost double the size of monomer domains in non-stressed nuclei
445 (Fig. 7A). However, as stress becomes more pronounced in 10 µm patterns, the dispersion of
446 Δ95-99 monomers recedes, with distributions in 499±250 nm domains (Fig. 7A). Thus, contrary
447 to wild-type emerin, a progressive dispersion of Δ95-99 monomers over increasingly large INM
448 areas is not observed with growing mechanical stress, consistent with the abnormal changes in
449 NSI induced by the deletion. The formation of emerin oligomers remains very limited, with Δ95-
450 99 molecular densities increasing slightly from 1.3±0.1 to 1.7±0.1 and 2.0±0.1 fold above
451 random in 15 µm and 10 µm micropatterns (Fig. 7A; Table S2). With the concurrent
452 enlargement of nanodomains from 48±14 nm to 81±16 nm and 75±20 nm, the relative
453 oligomerization of Δ95-99 compared to non-mechanically stressed nuclei increases by 3.9 fold
454 initially, but does not rise further as nuclear stress intensifies (Fig. 7B). Δ95-99 oligomeric
455 nanodomains remain sparser and significantly less dense than for wild-type emerin in cluster
456 maps of nuclei under stress (Fig. 7C). Thus, the failure of Δ95-99 to gradually self-associate at
457 sufficiently high molecular densities leads to defective nuclear responses to force. This
458 underlines the importance of modulating the oligomerization of emerin as a function of
459 mechanical stress intensity for adaptive nuclear deformations.

460

461 **Discussion**

15

462   Combining single molecule imaging and quantitative measurements, we showed that emerin

463   distributes as monomers and oligomers at the INM and that clinically relevant EDMD mutations

464   induce modified emerin mobility and nanoscale organizations. The oligomerization of emerin is

465   modulated by its ability to engage or disengage interactions with various structural elements

466   juxtaposed to the INM, including lamin A/C, SUN1, nuclear actin and BAF. Regulated

467   expressions of lamin A/C and SUN1, together with functional LINC complexes, are essential for

468   the formation and the stabilization of emerin oligomers, while balanced interactions of emerin

469   with BAF and nuclear actin further modulate its diffusion and its oligomerization potential. We

470   also showed that the mechanotransducing functions of emerin are coupled to its oligomeric state,

471   with the formation and maintenance of emerin oligomers being central to nuclear shape

472   adaptation against forces. Indeed, EDMD-inducing mutations that affect the self-assembly of

473   emerin and its binding to structural elements at the INM lead to abnormal nuclear deformations

474   and defective nucleus positioning in response to mechanical stress.

475   While the altered in vitro binding properties of Q133H, Δ95-99 and P183H emerin mutants result

476   in expected differences in organization in cells, they do not necessarily induce fully predicable

477   changes in diffusion and distribution at the NE. In effect, via its flexible IDR, emerin appears to

478   mediate complex interactions with itself, lamin A/C, SUN1, nuclear actin and BAF, where

479   binding to one partner impacts oligomerization and, interdependently, affects interactions with

480   other partners. As shown from the organization of wild-type emerin after nuclear actin depletion

481   or accumulation and our study of Q133H emerin, binding to nuclear actin significantly

482   influences the mobility and the oligomerization potential of emerin. Actin binding to the IDR of

483   emerin could mask interaction domains that normally serve as LEM binding and self-association

484   sites between emerin monomers(Berk et al., 2014). IDR masking, combined with the reduced

485   lateral mobility of actin-bound emerin, might therefore modulate the formation of oligomers by

486   limiting molecular collisions between emerin monomers. Consistent with the need to precisely

487   adjust the oligomerization potential of emerin for adaptive nuclear shape deformations, increased

488   emerin diffusion and controlled formation of emerin oligomers are coupled molecular events

489   during nuclear adaptation against stress, as shown by our measurements in micropatterns. We

490   thus speculate that the deficient binding of Q133H emerin to nuclear actin and its over-

491   oligomerization at SUN1 LINC complexes are linked to the abnormal nuclear deformations

492   observed in cells.

16

493   The differential interactions of emerin with its nucleoplasmic partners and their influence on its

494   mobility and its oligomerization are also underlined by the surprisingly slow mobility of Δ95-99

495   emerin, which does not bind lamin A/C nor actin in vitro, but binds BAF. The 48-118 region of

496   emerin, where Δ95-99 is located, was suggested to act as a binding site for the LEM

497   domain(Berk et al., 2014) and through altered region flexibility, the deletion might reduce the

498   efficacy of such interactions, potentially causing the LEM domain to bind BAF more

499   frequently(Samson et al., 2017). Repeated interactions of Δ95-99 with BAF and, indirectly, with

500   the lamina or chromatin via ternary BAF complexes, could slow its diffusion, limit molecular

501   collisions, and impede its oligomerization by sequestering the LEM domain and reducing

502   bridging interactions with LEM binding sites on other emerin. The Δ95-99 deletion, within the

503   55-132 lamin tail-binding region of emerin(Berk et al., 2014), could also prevent a stabilization

504   of already sparse Δ95-99 oligomers by direct lamin A/C binding. We thus postulate that the

505   aberrant nuclear deformations against stress of cells expressing Δ95-99 emerin stem from out of

506   balance interactions of this mutant with BAF and its inability to form lamin A/C-stabilized

507   oligomers at SUN1 LINC complexes.

508   A similar impediment of *in trans* interactions between the LEM domain and self-association sites

509   along the joined IDR of P183H dimers likely result in their reduced ability to oligomerize,

510   despite retained binding to lamin A/C and SUN1. The reported enhanced binding of lamin A/C

511   to P183H emerin(Lee et al., 2001), in close proximity to these same self-association sites could

512   also interfere with inter-emerin bridging interactions. In both cases, the inability of the LEM

513   domain to access binding sites along the IDR would elicit its repeated interactions with BAF,

514   leading to the observed slow diffusion of P183H at the INM. The defective nuclear shape

515   adaptation to mechanical challenges of cells expressing P183H might thus arise from emerin

516   dimerization and excessive interactions with BAF or lamin A/C that prevent an efficient

517   formation of emerin oligomers at LINC complexes. Our observation that lamin A/C

518   overexpression, which was previously shown to induce the nuclear accumulation of BAF(Loi et

519   al., 2016), leads to the decreased oligomerization of wild-type emerin is indeed consistent with

520   the need to modulate emerin/BAF/lamin A/C tripartite interactions to promote the self-assembly

521   of emerin.

522   As we have shown, because Δ95-99 emerin does not self-assemble into sufficiently dense

523   oligomers at the INM, it induces aberrant nuclear shape remodeling against mechanical stress.

524 The phosphorylation of emerin residues Tyr 74 and Tyr 95 was previously shown to mediate the
525 recruitment of lamin A/C to the LINC complex during nuclear stiffening in response to
526 force(Guilluy et al., 2014). Our observation that Δ95-99 fails at promoting adaptive nuclear
527 deformation in response to mechanical cues by its reduced ability to form lamin A/C- and SUN1-
528 stabilized oligomers is consistent with the major role played by Tyr 95 phosphorylation for
529 emerin-mediated mechanotransduction at the NE. The abnormal organization of cytoskeletal
530 actin in mechanically challenged cells expressing Δ95-99, akin to disorganizations detected with
531 a non-phosphorylable tyrosine 74-95FF emerin(Guilluy et al., 2014), also suggests that emerin
532 oligomers strengthen the connection between lamin A/C, the LINC complex and cytoskeletal
533 filaments to promote correct nucleus positioning and deformation. These data point towards a
534 link between Tyr 95 phosphorylation, emerin oligomerization and recruitment of lamin A/C for
535 stiffening the NE at LINC complexes, likely driven by phosphorylation-induced changes in
536 emerin conformation(Berk et al., 2013a; Tifft et al., 2009). It is thus possible that emerin
537 oligomeric nanodomains are enriched in Tyr 95 phosphorylated emerin, lamin A/C and LINC
538 complex components, while emerin monomers populate the rest of the INM, consistent with
539 emerin enrichments in distinct nucleoskeletal "niches" at the NE(Berk et al., 2013a).

540 Taken together, these lines of evidence support a model in which, during stress responses,
541 transient unbinding of emerin monomers from nuclear actin and BAF favors oligomerization by
542 increasing the lateral diffusion of emerin at the INM and exposing both its LEM domain and
543 self-association sites along its IDR for intermolecular binding between emerin at LINC
544 complexes (Fig. 8). Within emerin oligomers, stabilization by direct interactions with lamin A/C
545 and SUN1 and additional modulation of emerin self-association by nuclear actin and BAF likely
546 allow for a precise regulation of the oligomerization potential and the size of emerin oligomeric
547 nanodomains at LINC complexes, as required for adaptive nuclear deformation in response to
548 forces transmitted by cytoskeletal filaments. The localized INM distribution of emerin
549 oligomers, the involvement of lamin A/C and SUN1 in their stabilization, their specific
550 disruption following LINC complex destabilization, and their reliance on a part of the emerin
551 IDR that requires phosphorylation for the recruitment of lamin A/C to LINC complexes(Guilluy
552 et al., 2014), indeed support the idea that they are sites where interactions between emerin, lamin
553 A/C and LINC components are strengthened. It was recently suggested that the clustering of
554 SUN proteins could enable them to sustain high mechanical loads at the NE during force-

555   dependent processes(Jahed et al., 2018). Emerin oligomerization at SUN1 LINC complexes,

556   might therefore contribute to the increased connectivity between the nucleoskeleton, the NE and

557   the cytoskeleton for anchoring the nucleus and providing force absorption contact points during

558   nuclear deformation.

559   In response to surging mechanical stress, the incremental oligomerization of emerin in enlarged

560   nanodomains we observed could be part of a mechanism that redistributes increasing forces over

561   wider areas at LINC complexes to maintain a basal membrane pressure at these anchoring points

562   between the nucleoskeleton, the NE and the cytoskeleton. Beyond this central role played by

563   emerin self-assemblies, emerin might have additional functions outside these anchoring

564   oligomeric nanodomains. For instance, the disengagement of emerin monomers from nuclear

565   actin likely reduces NE contacts with the nucleoskeleton, while some membrane connectivity

566   with nuclear chromatin is maintained, via BAF. Indeed, both the nucleoskeleton and chromatin

567   tethering to the NE participate in nuclear mechanics(Stephens et al., 2017). Together,

568   strengthening the connections between the NE, the lamina and the cytoskeleton at LINC

569   complexes, but partially relaxing them in the rest of the membrane could provide means to

570   couple controlled nuclear deformation with nucleus positioning in cells. As we showed, such

571   coupling is defective with emerin mutants.

572   Additional cross-correlative studies will be needed to further define how the structural

573   interdependencies between emerin monomers, emerin oligomers, SUN1, BAF, and key

574   nucleoskeletal elements spatially regulate INM/lamina and INM/chromatin contacts and

575   reinforce the connections between the NE and the cytoskeleton at LINC complexes during

576   nuclear responses to force. At the center of these processes, emerin diffusion and

577   monomer/oligomer exchanges provide a means to transduced mechanical cues throughout the

578   entire NE, for coordinated changes in local nuclear stiffness and remodeling of the nuclear shape.

579

580

581   ## Materials and Methods

582   **Cell culture, emerin expression and cell staining**

583   Emerin-null human dermal fibroblast ($EMD^{-/y}$ HDF) and normal dermal fibroblasts ($EMD^{+/y}$

584   HDF) were kindly provided by Dr. Howard Worman, Columbia University, USA, and regularly

585   tested for contaminations. $EMD^{-/y}$ HDF are derived from a male EDMD patient (G-9054) and

586   carry a 59 nucleotide deletion within the *EMD* gene (*EMD* g.329del59) that ablates emerin

587   expression(Talkop et al., 2002). HDF were grown in DMEM (Lonza) with 10% fetal bovine

588   serum (Gibco-Life Technologies), 50 units ml^{-1} penicillin and 50 μg ml^{-1} streptomycin and

589   maintained at 37°C in a humidified atmosphere with 5% CO_2.

590   Human wild-type emerin cDNA was kindly provided by Dr. Juliet Ellis, University College

591   London, UK. For the expression of PA-TagRFP-emerin, a pEGFP-N1 plasmid backbone

592   encoding emerin fused to the C-terminus of PA-TagRFP was produced by XbaI and KpnI

593   insertion and PCR fusion of the human emerin cDNA. Cells plated on fibronectin-coated glass

594   coverslips were transfected with PA-TagRFP-emerin using X-tremeGENE HP (Roche). 48-72

595   hours post-transfection, live cells were imaged by sptPALM in HBSS buffer at 37°C. For

596   micropatterning experiments, cells grown on 6-well plates were trypsinized after 48-72 hours of

597   transfection and plated on fibronectin-micropatterned coverslips.

598   To express SNAP-emerin, human emerin was first fused to the C-terminus of a SNAP tag by

599   AscI and XhoI insertion in a pSNAP-tag(m) plasmid (NEB). SNAP-emerin was then subcloned

600   into a modified pFUW lentiviral vector by NheI and AgeI insertion. Lentiviral particles for the

601   expression SNAP-emerin were produced by the UCLA Vector Core. Transduction of HDF

602   grown at 70% confluence on 6-well plates was done for 48 hours, using 25 ng ml^{-1} of lentiviral

603   particles in complete growth medium containing 8 μg ml^{-1} of polybrene, after which the medium

604   was replaced. Following another 24 hours incubation, cells were trypsinized, and plated on

605   fibronectin-coated or fibronectin-micropatterned coverslips. For imaging, cells were fixed with

606   4% paraformaldehyde in PBS for 15 min, permeabilized with 0.1% Triton X-100 (Sigma-

607   Aldrich) for 15 min and blocked with 4% bovine serum albumin (BSA, Sigma-Aldrich) + 0.1%

608   Tween-20 (Sigma-Aldrich) for 30 min, at room temperature. Cells were then stained with 1 μM

609   of SNAP-Surface-AlexaFluor 647 (BG-A647, NEB) in 4% BSA + 0.1% Tween-20 for 1 hour at

610   37°C, then thoroughly washed before super-resolution imaging.

611   For the expression of sGFP-emerin, humanized cDNA for split-GFP 1-10(Pinaud and Dahan,

612   2011) was inserted by NheI and XbaI digestion in the pEGFP-N1 plasmid backbone encoding

613   emerin, and expressed as an N-terminal fusion to emerin. The shorter 11th β-sheet M3

614   fragment(Pinaud and Dahan, 2011) was also fused to the N-terminus of emerin by PCR cloning

615   using primers encoding the M3 fragment sequence and subcloning into the pEGFP-N1 backbone

20

via NheI and XhoI digestions. Both plasmids were co-transfected in HDF using X-tremeGENE HP (Roche) as described for PA-TagRFP-emerin, and cells were imaged by CALM 48-72 hours post-transfection. All constructs were verified by sequencing.

For immunostaining of emerin, cells were grown on coverslips, fixed and permeabilized as described for SNAP-emerin staining. Cells were labeled with a rabbit anti-emerin antibody (1:500, Santa Cruz Biotechnology, sc-15378) for 45 min, washed in PBS and further labeled with a goat anti-rabbit Alexa fluor 488 antibody (1:400, Invitrogen) for 45 min. After washing, cells were mounted in a DAPI-Fluoromount G (Electron Microscopy Sciences) and imaged by confocal microscopy.

To label cytoplasmic actin and measure nuclear shape indices, cells were fixed with 4% paraformaldehyde in PBS for 15 min, permeabilized with 0.1% Triton X-100 for 10 min, and blocked with 4% bovine serum albumin + 0.1% Tween-20 for 1 hour. Cells were stained with phalloidin-iFluor 488 (1:1000, Abcam) for 1 hour, washed with PBS, mounted in DAPI-Fluoromount G and imaged by confocal or wide field microscopy.

Mutations, siRNA and exogenous protein expressions

Emerin mutations Q133H and P183H were introduced in PA-TagRFP-emerin, SNAP-emerin, and emerin fused to both split-GFP fragments by site-directed mutagenesis using QuickChange Lightning Site Directed Mutagenesis (Agilent) and mutagenic primer pairs for:

Q133H: 5'-CGCTTTCCATCACCATGTGCATGATGA-3' and

                     5'-GATCGTCATCATGCACATGGTGATGGA-3'

P183H: 5'-CCTGTCCTATTATCATACTTCCTCCTC-3' and

                     5'-GTGGAGGAGGAAGTATGATAATAGGA-3'.

The Δ95-99 emerin deletion was produced using partially phosphorothioated PCR primers and T7 exonuclease digestion, as previously described(Stoynova et al., 2004). Primers pairs for the Δ95-99 deletion were:

                     5'-GACTACTTCACCA*C*C*A*GGACTTAT-3' and

                     5'-GGTGAAGTAGTCG*T*C*A*TTGTAGCC-3',

where * denotes phosphorothioate modifications. All primers were obtained from Integrated DNA Technologies (IDT) and all mutations were verified by sequencing.

646 siRNA duplex for BAF, SUN1 and Dicer siRNA for lamin A/C, SUN1 and controls were

647 obtained from IDT. The sequences of sense nucleotides were as follows:

648   - BAF siRNA: 5'-AGAUUGCUAUUGUCGUACUUU-3'

649   - Lamin A/C DsiRNA #1: 5'-AGCUGAAAGCGCGCAAUACCAAGaa-3',

650   - Lamin A/C DsiRNA #2: 5'-GGAACUGGACUUCCAGAAGAACAtc-3',

651   - SUN1 DsiRNA #1 5'-GCUUUUAGUAUCAACCACGUGUCaa-3'.

652   - SUN1 siRNA #2: 5'-CCAUCCUGAGUAUACCUGUCUGUAU-3'.

653   - Control DsiRNA: 5'-CGUUAAUCGCGUAUAAUACGCGUat-3' (IDT#51-01-14-

654   04).

655 siRNA duplex for IPO9 was obtained from Ambion (id# S31299) and siRNA for the nuclear

656 actin exporter XPO6 was obtained from Qiagen (id# SI00764099). All siRNA were transfected

657 or co-transfected with emerin plasmids at 25 nM using X-tremeGENE HP (Roche). When

658 associated with lentiviral expression of emerin, siRNA transfection was done 2 hours before viral

659 titer application.

660 Exogenous BAF^{L58R} was expressed from an EGFP-BAF^{L58R} lentiviral plasmid(Samwer et al.,

661 2017) and lentiviral particles were produced by the UCLA Vector Core. HDF cells were

662 transduced with 25 ng ml^{-1} of lentiviral particles as described for SNAP-emerin. For rescue of

663 lamin A/C expression and overexpression experiments, cDNA encoding for an exogenous

664 siRNA-resistant human lamin A/C (Frock et al., 2006) was kindly provided by Dr. Richard

665 Frock, Stanford University, USA and used together with lamin A/C DsiRNA #2, designed to

666 knockdown endogenous lamin A/C. For rescue of SUN1 expression and overexpression

667 experiments, cDNA encoding for an exogenous siRNA-resistant human SUN1 fusion to EGFP

668 (EGFP-SUN1) was kindly provided by Dr. Christine Doucet, Centre de Biochimie Structurale,

669 Montpellier, France and used together SUN1 siRNA #2, designed to knockdown endogenous

670 SUN1, as previously described(Talamas and Hetzer, 2011). Exogenous expression of mcherry-

671 DN-KASH was achieved by cell transfection of the mammalian expression plasmid #125553,

672 obtained from Addgene.

673

674 **Cell micropatterning and nuclear shape index measurements**

675 HDF were micropatterned as described previously(Bautista et al., 2019; Fernandez et al., 2017).

676 Briefly, hexamethyldisilazane-activated glass coverslips (Marienfeld, #1.5, Ø25 mm) were

22

677   stamped with rectangular and fibronectin-coated polydimethylsiloxane stamps having lengths of

678   210 µm and widths of 15 µm, 10 µm, or 5 µm respectively. Cell attachment outside the

679   fibronectin strips was blocked with a 1% solution of Pluronic F-127. After attachment for 1 hour

680   and removal of unattached cells, HDF were allowed to spread out on the micropatterns for 6

681   hours at 37°C before being prepared for microscopy imaging.

682   Using ImageJ(Schneider et al., 2012), the nuclear shape index (NSI) was determined by

683   measuring the nuclear cross-sectional area and the nuclear perimeter of DAPI-stained nuclei

684   imaged by wide-field microscopy, and by calculating the ratio:

685    $$\text{NSI} = \frac{4 \times \pi \times \text{area}}{\text{perimeter}^2} \qquad (1)$$

686   The NSI measures the roundness of the nucleus, with an NSI of 1 corresponding to a circular

687   nuclear shape. Mean NSI values ± standard deviation of the mean were reported for multiple cell

688   nuclei per condition. In graphs, the box length indicates the NSI interquartile range, the central

689   square indicates the NSI mean, the central bar indicates the NSI median and the error bars

690   indicate the standard deviation. The number of measured nuclei was n=54, 70, 61 and 62 nuclei

691   for $EMD^{+/y}$ cells in non-patterned, 15, 10 and 5 µm wide patterns, respectively; n=75, 60, 70 and

692   66 nuclei for lamin A/C depleted cells; and n=62, 71, 66 and 46 nuclei for nuclear actin depleted

693   cells. For $EMD^{-/y}$ cell expressing wild-type emerin, the number of measured nuclei was n=38,

694   33, 26 and 57 nuclei in non-patterned, 15, 10 and 5 µm wide patterns, respectively; n= 74, 58 and

695   37 nuclei for Q133H emerin; n= 64, 89, 45 and 46 nuclei for Δ95-99 emerin and n=82, 78 and 28

696   nuclei for P183H emerin. Significant differences between NSI values were evaluated using a

697   Wilcoxon rank-sum test.

698

699   **Microscopy imaging**

700   Confocal imaging of immunostained emerin in normal HDF, emerin-null HDF and emerin null

701   HDF after expression of wild-type PA-TagRFP-emerin were performed on an Olympus

702   Fluoview FV1000 confocal microscope equipped with a 60x/1.40 NA objective, 405 nm and 488

703   nm lasers and appropriate emission filters for imaging DAPI (450/20 nm) and Alexa-488 labeled

704   antibodies against emerin (510/10 nm).

705   Confocal imaging of nuclear deformation and actin organization in micropatterned $EMD^{+/y}$ HDF

706   was performed on a Zeiss LSM 700 microscope equipped with a C-Apochromat 63×/1.15 W

23

707 Korr objective, excitation lasers at 405 nm and 488 nm and appropriate beamsplitter and

708 emission channel settings for dual detection of DAPI and phalloidin-iFluor 488.

709 Wide-field imaging of labeled actin and labeled nuclei for NSI measurements were performed on

710 an inverted Nikon Eclipse Ti-E microscope equipped with a 40x objective (Nikon), an iXon

711 Ultra EMCCD camera (Andor), 405 nm and 488 nm lasers, a T495lpxr dichroic mirror and a

712 525/50 emission filter (Chroma) for phalloidin-iFluor 488 or a 458Di02 dichroic mirror and a

713 483/32 emission filter (Semrock) for DAPI.

714 SptPALM, dSTORM and CALM imaging were performed on an inverted Nikon Eclipse Ti-E

715 microscope equipped with a 100x 1.49 NA objective (Nikon), an iXon EMCCD camera (Andor),

716 perfect focus drift compensation optics, an astigmatic lens for 3D super-resolution imaging, a

717 piezo z-scanner for calibration of 3D super-resolution images (Mad City Labs), laser lines at 405,

718 488, 561 and 647 nm (Agilent), a multiband pass ZET405/488/561/647x excitation filter

719 (Chroma), a quad-band ZT405/488/561/647 dichroic mirror (Chroma) and appropriate emission

720 filters for sptPALM imaging of PA-tagRFP (600/50 nm, Chroma), 3D-dSTORM imaging of

721 Alexa-647 (700/75 nm, Chroma) and CALM imaging of complemented split-GFP (525/50 nm,

722 Semrock).

723 sptPALM of PA-TagRFP-emerin was performed in 37ºC HBSS buffer (Corning) by highly

724 inclined and laminated optical sheet (HILO) excitation of the bottom nuclear membrane of cells

725 with a continuous and low power photoactivation at 405 nm and an excitation at 561 nm. The

726 HILO illumination angle was $\theta= 51.6º$. Images were acquired continuously at a frame rate of 40

727 ms per frame for no longer than 3 minutes per cell to limit UV damage. CALM imaging of

728 complemented emerin-GFP-emerin species was done as described for sptPALM but with a single

729 HILO excitation at 488 nm.

730 dSTORM of SNAP-emerin labeled with BG-A647 was performed at room temperature in a

731 photoswitching buffer composed of 10% glucose, 0.5 mg ml^{-1} glucose oxidase (Sigma), 40 μg

732 ml^{-1} catalase (Sigma), and 1% β-mercaptoethanol (Sigma). Continuous photoswitching was

733 achieved with a low power 488 nm laser and imaging was done with a 647 nm laser excitation at

734 a frame rate of 80 ms per frame. Z-calibration and sample drift corrections were done using a

735 few 40 nm TransFluoSphere beads (488/685 nm, Life Technologies) as fiducial markers spread

736 on the cell samples.

24

737   For rescue and overexpression experiments, dSTORM imaging of SNAP-emerin was performed

738   only in cells expressing exogenous human lamin A/C, human EGFP-SUN1 or mcherry-DN-

739   KASH, as identified by lamin A/C immunostaining, EGFP or mCherry fluorescence. In the case

740   of lamin A/C and EGFP-SUN1 rescues, imaging was done in cells having relatively low

741   exogenous expressions.

742

743   **Fluorescence recovery after photobleaching (FRAP) of emerin:** FRAP of wild-type emerin

744   and emerin mutants was done in U2OS cells transiently transfected with PA-TagRFP-emerin.

745   Cells were imaged at 37ºC in HBSS buffer (Corning) on an Olympus Fluoview FV1000 confocal

746   microscope equipped with a 60x/1.40 NA oil immersion objective. PA-TagRFP-emerin at the

747   bottom NE was briefly photoactivated by laser scanning at 405 nm and PA-TagRFP fluorescence

748   was monitored every 2.8 seconds with a 543 nm laser. Circular regions of interest (7 µm in

749   diameter) were photobleached and recorded. After background subtraction, FRAP curves were

750   doubly normalized as previously described(Phair et al., 2004) to correct for loss of fluorescence

751   due to bleaching during acquisition. FRAP curves from measurements on 9-12 cells per

752   condition were averaged after normalization to full scale. After comparison of one- or two-

753   component lateral diffusion models(Soumpasis, 1983), the apparent diffusion coefficients of

754   emerin were determined by fitting FRAP curves with a two-component model using equations

755   for a uniform circular bleach region(Soumpasis, 1983). A fast ($D_{fast} = 4.48 \times 10^{-2} \pm 1.0 \times 10^{-2}$

756   $\mu m^2/s$, 17%) and slow ($D_{slow} = 4.0 \times 10^{-3} \pm 4 \times 10^{-4}$ $\mu m^2/s$, 83%) diffusive behaviors of wild-type

757   emerin is observed by FRAP (Fig. S1), consistent with previously diffusion values ($1.0 \times 10^{-1} \pm$

758   1×10^{-2} $\mu m^2/s$ and $7.50 \times 10^{-2} \pm 2.9 \times 10^{-3}$ $\mu m^2/s$)(Haraguchi et al., 2008; Ostlund et al., 1999;

759   Ostlund et al., 2006) and the reported presence of a nearly immobile emerin fraction at the

760   NE(Haraguchi et al., 2008; Shimi et al., 2004). Emerin mutations P183H, Q133H, and Δ95-99 do

761   not display statistically significant differences in ensemble diffusion dynamics compared to wild-

762   type emerin (Fig. S1).

763

764   **Cell extracts and immunoblotting:** After siRNA treatment, cells were harvested and

765   fractionated as described previously(Berk et al., 2013a). Cells were scraped, centrifuged for 5

766   min at 4000 g and washed three times with PBS. Cell pellets were then flash frozen and stored at

767   -80°C. Cells were thawed for 10 minutes on ice, and then for 10 min in 300 µl ice cold hypotonic

768   lysis buffer (20 mM HEPES, pH 7.4, 50 mM N-acetylglucosamine, 1 mM DTT, 100 µM PMSF,

769   1 µg/ml pepstatin A, 1x protease inhibitor (Roche) and 1x PhosSTOP phosphatase inhibitor

770   (Roche) before being resuspended and set on ice for another 10 min. Cells were then spun down

771   at 17,000 g for 1 min to collect the supernatant cytoplasmic fraction. The pellet was then washed

772   three times in PBS with spinning at 17,000 g for 1 min in between washes to remove any

773   residual cytoplasmic components. The pellet was then resuspended in nuclear lysis buffer (50

774   mM Tris-HCL, pH 7.4, 300 mM NaCl, 0.3% Triton X-100, 50 mM N-acetylglucosamine, 1 mM

775   DTT, 100 µM PMSF, 1 µg/ml pepstain A, 1x protease inhibitor (Roche) and 1x PhosSTOP

776   phosphatase inhibitor (Roche) before vortexing to release nuclear contents. Nuclear fractions

777   were additionally sonicated 20 times in 0.5 s bursts to liberate dense nuclear aggregates.

778   Cytoplasmic and nuclear fractions were analyzed by SDS-PAGE. Protein concentrations were

779   determined using a Bradord assay, and equal amounts of protein were loaded on gels before

780   running in a Laemmli Buffer. Proteins were transferred to a nitrocellulose membrane (Bio-Rad)

781   by wet transfer at 4°C. The membrane was then rinsed with Tris-buffered saline (TBS, pH 7.5)

782   and blocked with 5% milk in TBS for 1 hour. Membranes were probed with the following

783   primary antibodies: mouse anti-lamin A/C (1:1000, Santa Cruz Biotechnology, sc-7292), mouse

784   anti-actin (1:1000, Santa Cruz Biotechnology, sc-8432), mouse anti-BAF (1:1000, Santa Cruz

785   Biotechnology, sc-166324), rabbit anti-SUN1 (1:2000; HPA008346, Sigma-Aldrich), mouse

786   anti-histone H2A (1:1000, Santa Cruz Biotechnology, sc-515808) and mouse anti-GAPDH

787   (1:1000, GeneTex, GTX627408). A goat anti-mouse IgG (H+L) HRP conjugate (1:3000,

788   Invitrogen, 62-6520) and a goat anti-rabbit IgG (H+L) HRP conjugate (1:5000, Invitrogen, 65-

789   6120) were used as secondary antibodies. Blots were developed with SuperSignal West Femto

790   Maximum Sensitivity Substrate (Thermo) and imaged on a Chemidoc XRS+ (BioRad). All

791   assays were performed in triplicate and immunoblot quantification was done with ImageJ, using

792   t-tests for statical comparisons with wild-type (Fig. S2).

793

794   **Immunostaining and fluorescence imaging of RNAi effects and exogenous protein**

795   **expressions:** $EMD^{+/y}$ HDF were transfected with control siRNAs, or siRNAs against lamin A/C,

796   IPO9, BAF, and SUN1, respectively as described in Materials and Methods. Cell were fixed with

797   4% PFA in 1x PBS for 15 min, permeabilized with 0.1% Triton X-100 for 10 min, and blocked

798   with 4% BSA + 0.1% Tween-20 for 1h, all at RT. For lamin A/C and SUN1 immuno-staining,

799   cells were incubated with mouse anti-lamin A/C (1:400; sc-7292, Santa Cruz Biotechnology) and

800   rabbit anti-SUN1 (1:500; HPA008346, Sigma-Aldrich) for 1hr at RT, rinsed 3x with 1x PBS for

801   5 minutes each, then stained with goat anti-mouse-Alexa Fluor 647 (1:500, Life Technologies)

802   and goat anti-rabbit-Alexa Fluor 488 (1:500, Life Technologies) for 1hr at RT. Following 3x

803   PBS rinse, the coverslips were mounted in DAPI-Fluoromount G (Electron Microscopy

804   Sciences) and imaged. For BAF staining, cells were incubated with mouse anti-BAF (1:100; sc-

805   166324, Santa Cruz Biotechnology) for 2hr at RT, then with goat anti-mouse-Alexa Fluor 647

806   (1:500) for further 2hr. To assess the effect of BAF L58R re-expression on lamin A/C

807   organization, 24 hours after siRNA treatment against BAF, cells were transduced with the

808   lentivirus for EGFP-BAF L58R expression and fixed two days later, before staining for lamin

809   A/C as described above. To assess the influence of lamin A/C or EGFP-SUN1 expression on the

810   localization of endogenous emerin, $EMD^{+/y}$ HDF were fixed and immunostained with rabbit anti-

811   emerin (Abcam) and mouse anti-lamin A/C (Santa Cruz Biotechnology) antibodies as described

812   above. Confocal fluorescence imaging (Fig. S2 and S6) was performed on a Zeiss LSM 780

813   microscope equipped with a C-Apochromat 63×/1.15 W Korr objective, excitation lasers at 405

814   nm, 488 nm and 633 nm, and appropriate beam splitter and emission channel settings for

815   detection of DAPI, GFP, Alexa Fluor-488 and Alexa Fluor-647 labeled secondary antibodies.

816   Other than effective and specific knockdown of targeted protein expressions, there was no

817   obvious indirect or off-target effects of the different siRNA treatments on the organization other

818   studied proteins (Fig. S2).

819   To assess the influence of IPO9 and XPO6 siRNA on nuclear actin organization and content,

820   Utr230-EGFP-3xNLS (Utr230-EN, Addgene #58466) was subcloned into a pHR-SFFV lentiviral

821   plasmid backbone, viral particles were generated, and $EMD^{+/y}$ HDF cells were transduced with

822   25 ng ml-1 of lentiviral particles as described for SNAP-emerin. 10 µg/mL blasticidin S

823   (Invivogen) was used over 12 days to establish a stable cell line expressing Utr230-EN. Cells

824   were then transfected with 25 nM of control, IPO9 or XPO6 siRNAs, as described above, before

825   being fixed with 4% PFA for 15 minutes, rinsed 3x with 1xPBS, and mounted using

826   Fluoromount-G (Electron Microscopy Sciences). Confocal fluorescence imaging was performed

827   on a Zeiss LSM 780 upright microscope equipped with a Plan-Apochromat 40×/1.4 Oil

828   objective, excitation laser at 488 nm, and appropriate beam splitter and emission channel settings

829   for the detection of EGFP. From confocal images, cells were classified into three groups

830   depending on the nuclear localization pattern of Utr230-EN: (i) small puncta and diffuse, (ii)

831   diffuse or (iii) large foci, based on a similar previous classification(Belin et al., 2013). Data were

832   pooled from three independent assays for each condition.

833

834   **Quantification of ONM emerin fraction**. The fraction of ONM emerin in $EMD^{+/y}$ HDF was

835   quantified after saponin (ONM+ER emerin) or Triton X-100 (INM+ONM+ER emerin)

836   permeabilization and immunostaining with rabbit anti-emerin (1 µg/mL, ab40688, Abcam) and

837   mouse anti-lamin A/C (1:1000, sc-7292, Santa Cruz Biotechnology) antibodies, as previously

838   described(Bautista et al., 2019). Whole cell volumes were imaged by 3D confocal microscopy

839   and all the z-slices were combined into a single image by sum intensity z-slices projection.

840   Regions of interest were delineated to quantify emerin fluorescence intensities over the entire

841   cells (ROI1) or over the nucleus (ROI2) after background corrections. Nuclear ROI2 were

842   further corrected for ER emerin contributions by evaluating the mean ER-only emerin intensity

843   per area from ROI1-ROI2 intensities. Using a representative set of 20 cells for both saponin and

844   Triton X-100 treatments, the fraction of ONM emerin per cell was then calculated using:

845    $$\text{ONM fraction} = \text{ER}_{corrected} \ \text{ROI2}_{saponin(ONM)} \ / \ \text{ER}_{corrected} \ \text{ROI2}_{Triton \ X\text{-}100(INM+ONM)}$$

846   The mean ONM fraction of emerin at the NE was 13 ± 6 %, in good agreement with the levels of

847   ONM emerin detected in sptPALM experiments (Fig. S4).

848

849   **Analyses of diffusion coefficients**

850   Localization and tracking analyses were performed using the software package SLIMfast, which

851   uses multiple-target tracing algorithms(Serge et al., 2008) and was kindly provided by Christian

852   Ritcher and Jacob Piehler. Localizations were performed by 2D-gaussian fitting of the point-

853   spread-function of each activated PA-TagRFP-emerin or activated emerin-GFP-emerin species

854   in each frame. Localization precision was determined as previously described(Mortensen et al.,

855   2010; Thompson et al., 2002), and individual PA-TagRFP-emerin were localized with a

856   precision of 13 ± 5 nm. Diffusion trajectories were built by linking localizations frame to frame

857   and accounting for blinking statistics and local particle densities. Trajectories with fewer than

858   three steps were discarded. Diffusion coefficients were estimated using a probability density of

859   square displacement (PDSD) analysis(Schutz et al., 1997). For each time lag t, the PDSD curve

860   was fitted with the following model:

861

$$P(\vec{r}^2, t) = 1 - \sum_{i=1}^{n} a_i(t) e^{-r^2/r_i^2(t)} \qquad (2)$$

863

$$\sum_{i=1}^{n} a_i(t) = 1$$

864

where $r_i^2(t)$ is the square displacement and $a_i(t)$ is the population density of i numbers of diffusive behaviors at each time lag t. To limit the risks of overfitting or underfitting the PDSD curves and select an appropriate model for i numbers of diffusive behaviors in each data set, we used both an Akaike information criterion (AIC) and a Bayesian information criterion (BIC) after fitting PDSD with models where $1 \leq i \geq 5$. Square displacement curves ($r_i^2(t)$) were extracted from PDSD analyses and reported with error bars determined using $\frac{r_i^2}{\sqrt{N}}$, where N is the number of analyzed trajectories per time lag, as previously described(Schutz et al., 1997). Diffusion coefficients (D) representative of each behavior were determined by fitting each $r_i^2(t)$ curves over the first four time lags (t_1-t_4) using OriginPro 2020 software (OriginLab) and a 2D Brownian diffusion model with position error:

$$r^2 = 4Dt + 4\sigma^2 \qquad (3)$$

The numbers of trajectories and nuclei analyzed were: wild-type emerin (71004 trajectories, 14 nuclei); lamin A/C depletion (lamin A/C KD, 60569 trajectories,11 nuclei); nuclear actin depletion (IPO9 KD, 74501 trajectories, 17 nuclei); replacement of endogenous BAF with BAF^{L58R} (BAF KD + BAF^{L58R}, 62714 trajectories, 8 nuclei); complemented wild-type emerin-GFP-emerin species assessed by CALM (4833 trajectories, 13 nuclei); wild-type emerin after nuclear deformation on 15 µm (27266 trajectories, 10 nuclei); wild-type emerin after nuclear deformation on 10 µm wide micropatterns (12915 trajectories, 8 nuclei); Q133H emerin (105050 trajectories, 13 nuclei); Δ95-99 emerin (76944 trajectories,14 nuclei); P183H emerin (86529 trajectories, 21 nuclei); and complemented P183H emerin-GFP-emerin species assessed by CALM (10519 trajectories, 21 nuclei). All diffusion coefficients D are reported in µm^2 s^{-1} $\pm$ standard error of fit value ($\pm$s.e.m.). Statistical comparisons between D values were done using t-tests. Population percentages are derived from the averaged $a_i(t)$ values over the considered time lags.

To estimate the diffusion that might be expected for immobile PA-TagRFP-emerin (D$_{immobile}$) under our imaging and analytical conditions, we simulated immobilized PA-TagRFP emerin with

29

891 photophysical parameters similar to that of live cell acquisitions, using the software

892 Fluosim(Lagardère et al., 2020). After PDSD analysis with SLIMfast, $D_{immobile}$ was determined at

893 $1.7 \times 10^{-4} \pm 2 \times 10^{-5} \mu m^2 s^{-1}$.

894 Individual diffusion coefficients (D_i) were obtained by fitting the individual mean square

895 displacement (MSD) for each detected emerin over the first three time lags (t_1-t_3), using again a

896 2D Brownian diffusion model. Based on their individual D_i value, emerin trajectories were

897 grouped into four diffusion ranges ($D_{i1} > 0.1 \mu m^2 s^{-1}$, $0.1 < D_{i2} > 0.01 \mu m^2 s^{-1}$, $0.1 < D_{i3} > 0.001 \mu m^2$

898 s^{-1}, and $D_{i4} < 0.001 \mu m^2 s^{-1}$) and plotted as maps.

899

Spatial distribution and cluster analyses from super-resolution images

901 After 3D-dSTORM super-resolution imaging, the localization of individual emerin molecules

902 and z-position assignments were performed by Gaussian fitting using rapidSTORM (version

903 3.3.1)(Wolter et al., 2012). Sample drift and overcounting corrections for molecules appearing in

904 consecutive frames were done using PALMsiever(Pengo et al., 2015) and renderings of super-

905 resolved images were done using ImageJ. Localization precisions (σ) in the x, y, and z

906 dimensions were evaluated as previously described(Fernandez et al., 2017) and were σ_x:8.3 nm,

907 σ_y:13.0 nm, and σ_z:28.4 nm. 2D spatial pattern analyses of emerin distributions were performed

908 on 2 µm x 2 µm regions of interest (ROI) typically chosen in NE areas having homogenous z

909 ranges and away from the edges of nuclei, in order to limit 3D effects.

910 Emerin clustering was determined using an edge-corrected neighborhood density function (NDF)

911 as previously described(Fernandez et al., 2017). Briefly, the NDF is a pairwise-correlation

912 function similar to O-ring statistics that tallies the density of detected emerin within a ring of

913 outer radius r and width Δr located at a distance r from an emerin position in the ROI and for all

914 $r + \Delta r$ in the ROI. The density of emerin as a function of distance from an average emerin was

915 obtained with:

916
$$D_r = \frac{\sum N_r}{\sum A_r} \qquad (4)$$

917 where N_r is the number of neighbors and A_r is the area summed over all detected emerin. NDF

918 analyses were done over a 1µm distance on selected ROIs and with a fixed ring width of 10 nm

919 and a ring radius increasing by 10 nm steps. To average NDF statistics from multiple ROIs

920 across different nuclei and make them sample-size independent, D_r was further standardized by

921 dividing it by the mean density of detected emerin across the entire ROI. As such, an NDF value

922   at a given radius indicates the relative clustering of emerin as compared to the average density

923   across the entire sample. This relative NDF gives a value of 1 for a completely random spatial

924   distribution as determined by Monte Carlo simulations of random emerin distributions with area

925   and number of randomly seeded emerin equal to that of each experimental ROIs.

926   Relative NDF curves averaged across multiple ROIs and multiple nuclei were fitted with a

927   previously described model(Fernandez et al., 2017), which accounts for a distribution of cluster

928   lengths that includes two populations of emerin (monomer and oligomers) and for a probability

929   density of emerin in 2D clusters that decays approximately as an exponential function(Sengupta

930   et al., 2011):

931    $$\text{Relative NDF} = \{A_1 \times \exp\left(\frac{-r}{\varepsilon_1}\right) + A_2 \times \exp\left(\frac{-r}{\varepsilon_2}\right) + 1\} * g(r)^{PSF} \quad (5)$$

932   where, A is the clustering density, ε is the typical half-maximum cluster length, $*$ denotes a 2D

933   convolution, and $g(r)^{PSF}$ is the correlation function of the effective point spread function of

934   uncertainty in position determination for the dSTORM experiments. As described

935   previously(Fernandez et al., 2017), $g(r)^{PSF}$ corrects the NDF for contribution of multiple single

936   molecule appearances (blinking) to the overall spatial distribution. After fitting relative NDF

937   curves, the molecular density above random for emerin clusters are reported as $A \pm$ standard

938   error of the fit (±s.e.m) and their typical size as $2 \times \varepsilon \pm$ standard error of the fit and localization

939   precision (±s.e.m). Relative increases in emerin oligomer formation during nuclear stress were

940   determined by considering a circular shape of oligomer nanodomains and multiplying the area of

941   oligomerization by the measured molecular density.

942   The numbers of localization and nuclei analyzed were: wild-type emerin in untreated cells

943   (189331 localizations, 10 nuclei); after control siRNA transfection (n= 180546 localizations, 5

944   nuclei); after lamin A/C knockdown (178206 localizations, 6 nuclei); after lamin A/C

945   knockdown and exogenous expression of lamin A/C (118859 localizations, 6 nuclei); after IPO9

946   knockdown (225394 localizations, 9 nuclei); after replacement of endogenous BAF by BAF[L58R]

947   (90,241 localizations, 6 nuclei); after SUN1 knockdown (258300 localizations, 6 nuclei); after

948   SUN1 knockdown and exogenous expression of EGFP-SUN1 (85210 localizations, 5 nuclei);

949   after exogenous expression of mCherry-DN-KASH (392365 localizations, 5 nuclei); after

950   nuclear deformation on 15 µm wide micropatterns (151647 localizations, 10 nuclei); after

951   nuclear deformation on 10 µm wide micropatterns (56563 localizations, 6 nuclei); for Q133H

952   emerin (149340 localizations, 6 nuclei); for Δ95-99 emerin (208092 localizations, 8 nuclei); for

953   P183H emerin (138075 localizations, 6 nuclei); for Δ95-99 emerin after nuclear deformation on

954   15 µm wide micropatterns (138119 localizations, 5 nuclei); and for Δ95-99 emerin after nuclear

955   deformation on 10 µm wide micropatterns (135143 localizations, 6 nuclei).

956

957   **Cluster maps**

958   Cluster maps were generated from drift- and overcounting-corrected super-resolved emerin

959   positions by determining local cluster values around each emerin using the Getis and Franklin L

960   function(Getis and Franklin, 1987) in spPack(Perry, 2004) and for a distance of 25 nm. Spatial

961   positions in x and y, and cluster values were plotted as maps in MATLAB (MathWorks) using

962   the meshgrid and griddata functions, a 1 nm x 1 nm pixel size and the 'v4' option when

963   calculating pixel density values. The contour maps were generated using the countourf function

964   with 200 levels. In contour maps, values $L(r_{25})=25$ represent areas where emerin is randomly

965   distributed and $L(r_{25})=70$ values represent areas with emerin local density $(70/25)^2 = $ ~8-fold

966   higher than expected for a random distribution.

967

968

969

970

971   **Acknowledgements**

976

977   **Competing financial interests**

978   The authors declare no competing financial interests.

979

980

981

982

983

984

985

986

987

988

989

990
991
992
993
994
995
996
997
998
999
1000
1001
1002
1003
1004
1005
1006
1007
1008
1009
1010
1011
1012
1013

1014
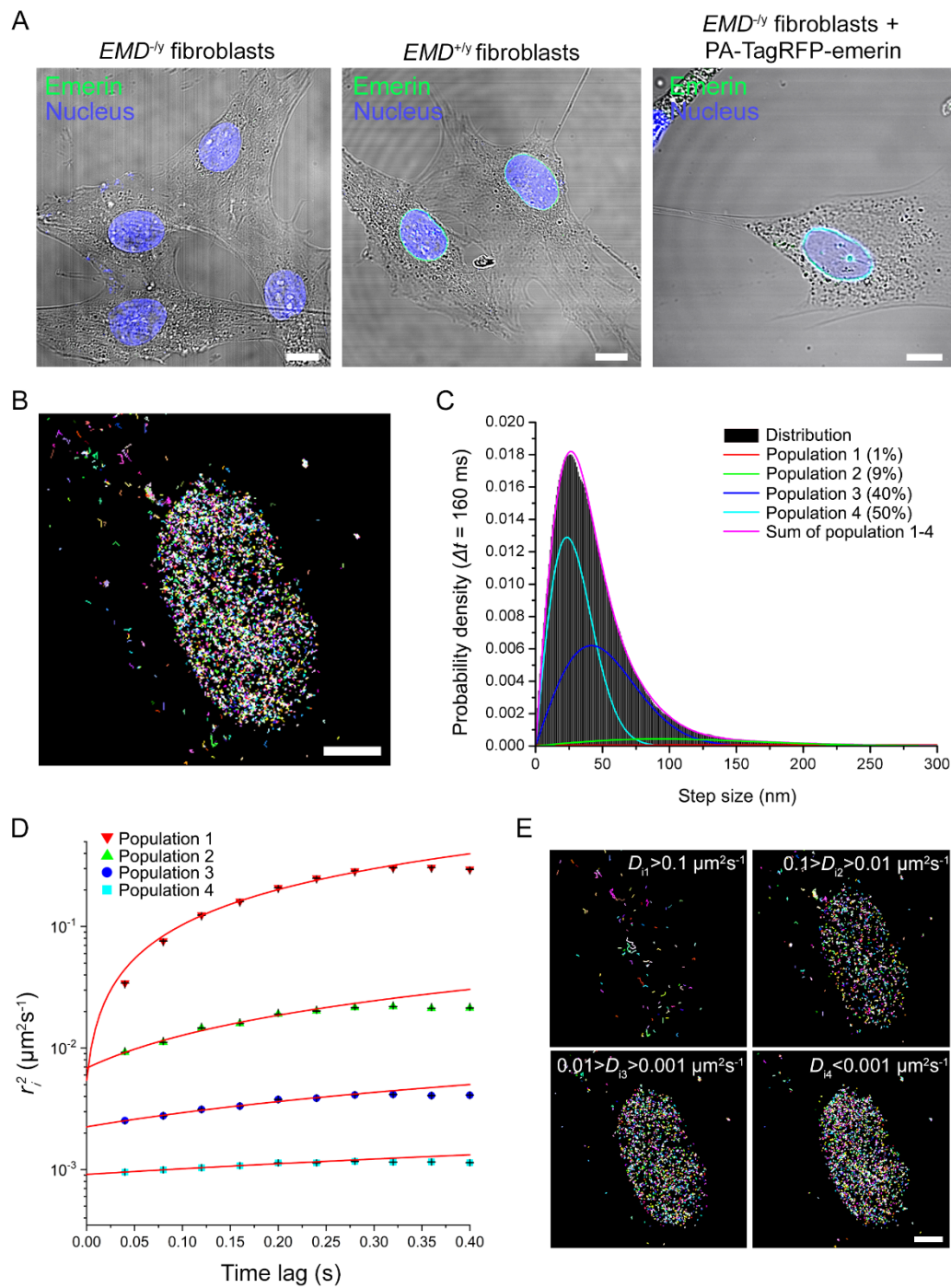
Fig. 1. **Emerin displays distinct diffusive behaviors at the nuclear envelope.** (A) Confocal imaging of emerin in $EMD^{-/y}$ HDF, $EMD^{+/y}$ HDF and $EMD^{-/y}$ HDF expressing wild-type PA-TagRFP-emerin. Scales: 10 µm. (B) Trajectory map of individual PA-TagRFP-emerin at the NE. Scale: 5 µm. (C) Probability distribution of square displacements for wild-type emerin at time lag Δt = 160 ms. (D) Square displacement curves (r^2_i) of each emerin diffusive behavior fitted over the first four values with a Brownian diffusion model (red line). (E) Emerin trajectory maps as a function of individual diffusion coefficient (D_i). Scale: 5 µm.

1022

34

1023
1024
1025

1026
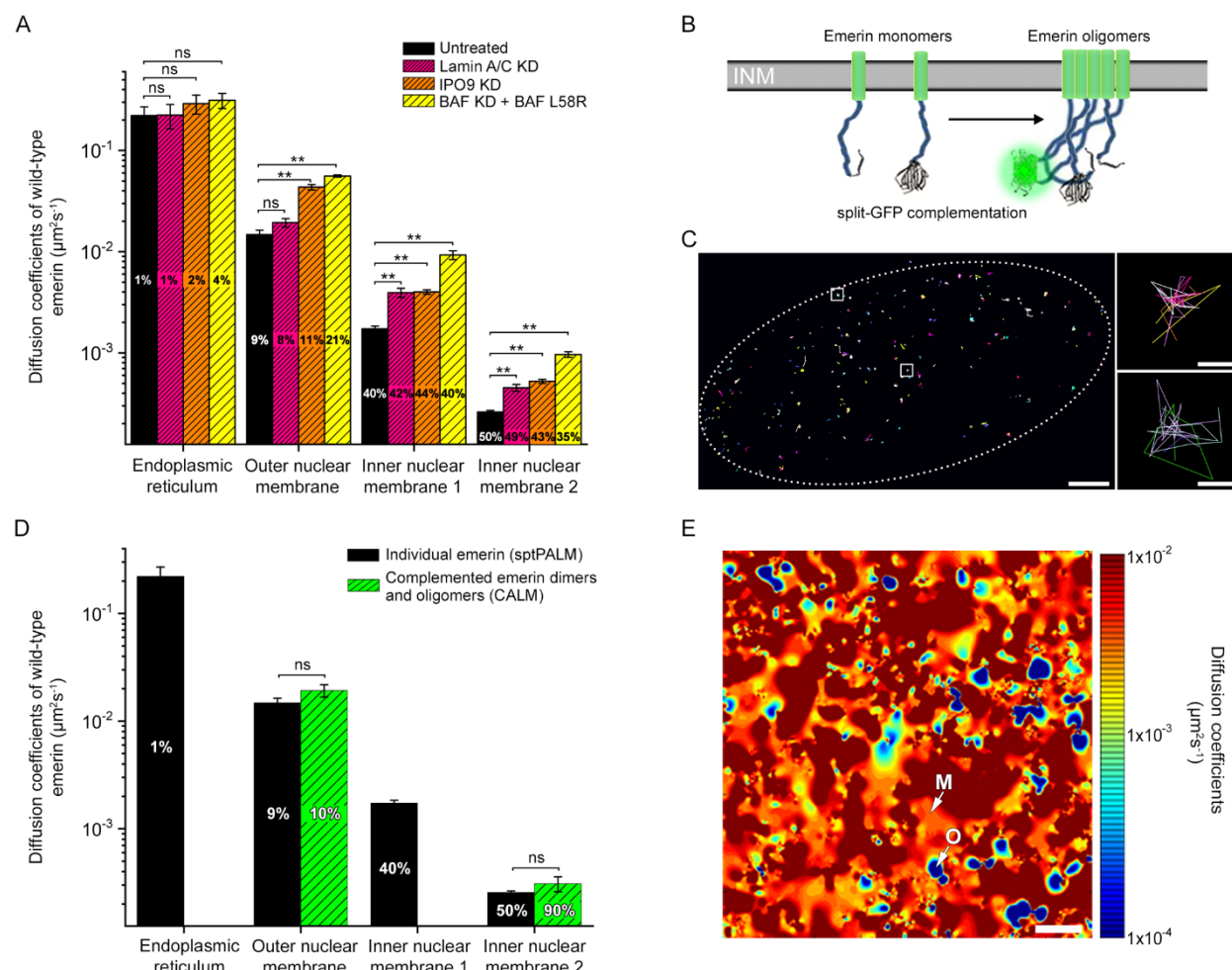
Fig. 2. Emerin diffuses as monomers and oligomers interacting with lamin A/C, nuclear actin and BAF. (A) Diffusion coefficients (±s.e.m.) and percentages of wild-type emerin after lamin A/C depletion, nuclear actin depletion (IPO9 KD) or replacement of endogenous BAF with BAF^{L58R}. (B) Schematic of emerin fusion to complementary split-GFP fragments. (C) Trajectory map of complemented emerin-GFP-emerin at the NE. Squares: oligomeric nanodomains with overlapping trajectories. Scales: 2 µm (left) and 50 nm (right). (D) Diffusion coefficients (±s.e.m.) and percentages for wild-type emerin assessed by sptPALM and complemented emerin-GFP-emerin species assessed by CALM. (E) Diffusion map of wild-type PA-TagRFP-emerin, showing slow mobility oligomeric domains (blue, O) surrounded by areas where emerin monomers diffuse faster (red, M). Scale: 500 nm. For (A, D): t-test, ns: non-significant, **: $p<0.01$.

1038

35

1039

1040

1041

1042

1043
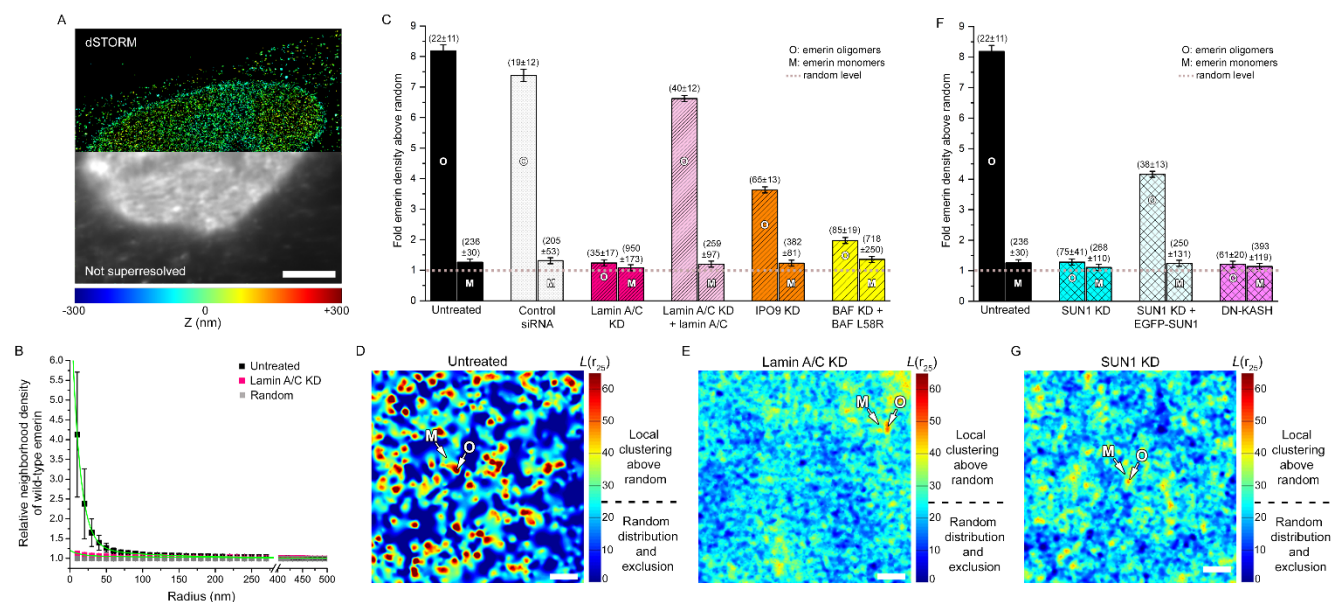
1044

Fig. 3. Emerin forms oligomeric nanodomains stabilized by lamin A/C and SUN1 at the LINC complex. (A) Super-resolved (top) and diffraction-limited imaging (bottom) of wild-type SNAP-emerin. Scale: 5 µm. (B) Neighborhood densities (±s.d.) at various length scales for wild-type emerin before and after lamin A/C knockdown, compared to complete spatial randomness. Fit shown in green. (C) Molecular densities above random (±s.e.m.) of wild-type emerin oligomers (O) and monomers (M) in untreated cells, after control siRNA, lamin A/C knockdown, lamin A/C knockdown and exogenous expression of lamin A/C, IPO9 knockdown to deplete nuclear actin or replacement of endogenous BAF by BAF^{L58R}. Values in parenthesis represent the size (±s.e.m.) of each domain in nanometers. (D) Local cluster map of wild-type emerin at the NE of an untreated HDF. (E) Local cluster map of wild-type emerin after lamin A/C knockdown. (F) Molecular densities above random (±s.e.m.) for wild-type emerin in untreated cells, after SUN1 knockdown, after SUN1 knockdown and exogenous expression of EGFP-SUN1 or after exogenous expression of mCherry-DN-KASH. (G) Local cluster map of wild-type emerin after SUN1 knockdown. For (D, E, G), M: monomer areas, O: oligomer nanodomains. Scales: 250 nm.
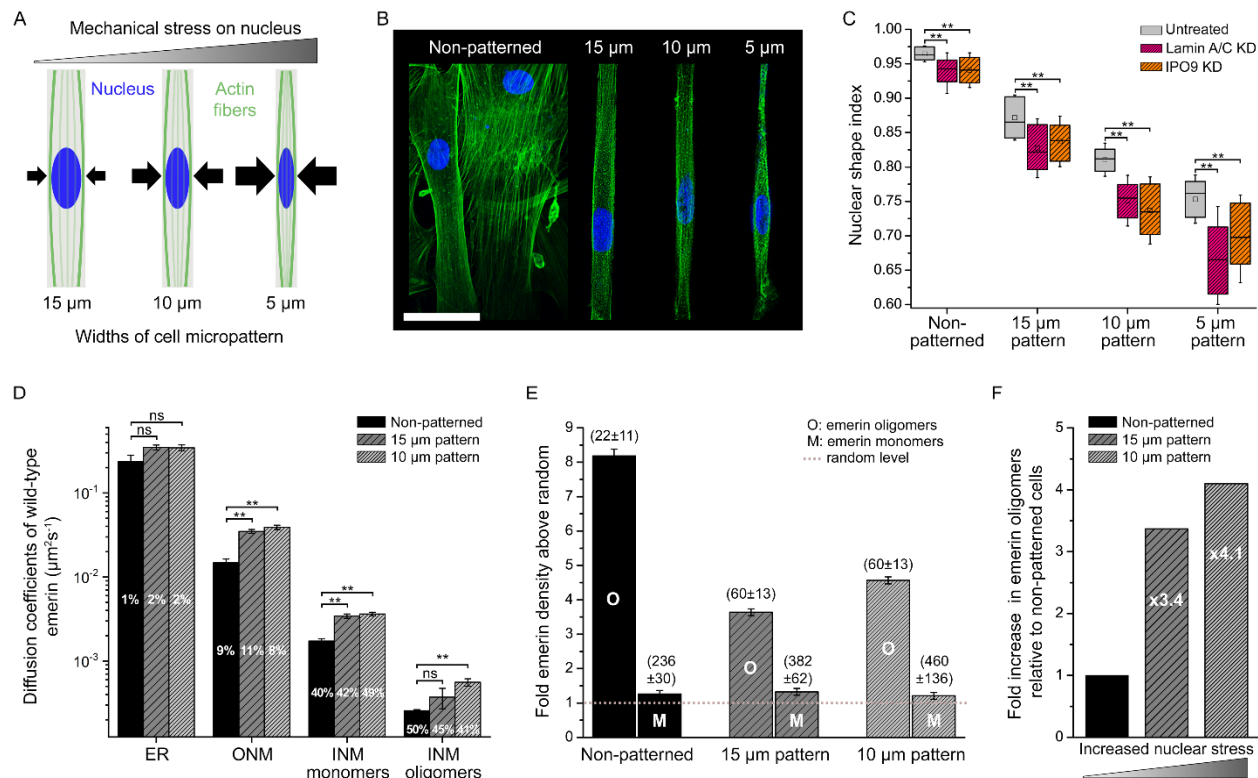
1060

36

Fig. 4. Mechanical stress increases emerin mobility and the formation of emerin oligomers.
(A) Schematic of increasing nuclear mechanical stress by cell micropatterning. Arrows represent force. (B) Confocal imaging of actin (green) and the nucleus (blue) in micropatterned $EMD^{+/y}$ HDF. Scale: 50 µm. (C) Nuclear shape index as a function of micropattern width in $EMD^{+/y}$ HDF depleted for lamin A/C or nuclear actin. Wilcoxon test, **: p<0.01. (D) Diffusion coefficients (±s.e.m.) and percentages of wild-type emerin in non-patterned cells or after nuclear deformation on 15 and 10 µm micropatterns. t-test, ns: non-significant, **: p<0.01. (E) Molecular densities above random (±s.e.m.) for wild-type emerin oligomers (O) and monomers (M) in non-patterned $EMD^{-/y}$ HDF and after nuclear deformation on 15 and 10 µm micropatterns. Values in parenthesis represent the size (±s.e.m.) of each domain in nanometers. (F) Increase in emerin oligomers as a function of nuclear stress.
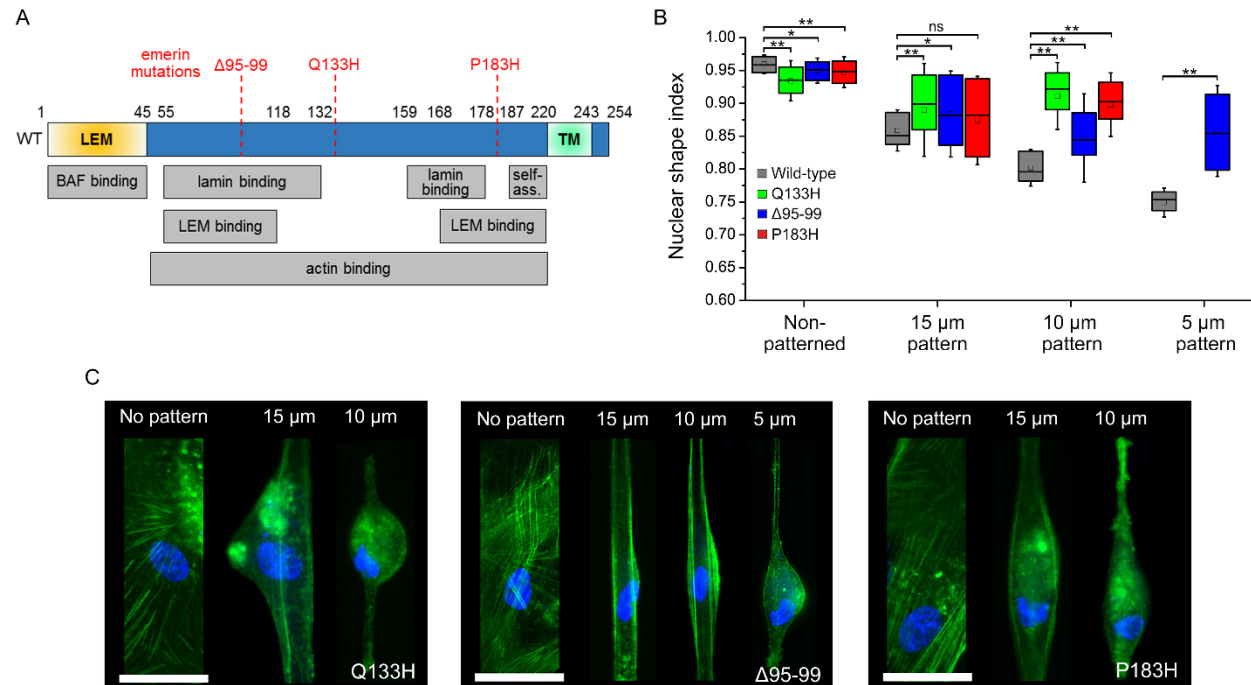
37

1074
1075

1076

Fig. 5. Emerin mutations induce defective nuclear shape adaptation against mechanical stress. (A) Diagram of emerin with binding and self-association domains (self-ass.) and position of Δ95-99, Q133H and P183H mutations. (B) Nuclear shape index as a function of micropattern width for $EMD^{-/y}$ HDF expressing wild-type, Q133H, Δ95-99 or P183H emerin. Wilcoxon test, ns: non-significant, *: $p<0.05$, **: $p<0.01$. (C) Fluorescence imaging of actin (green) and the nucleus (blue) in micropatterned $EMD^{-/y}$ HDF expressing Q133H, Δ95-99 or P183H emerin. Scales: 50 µm.

1084
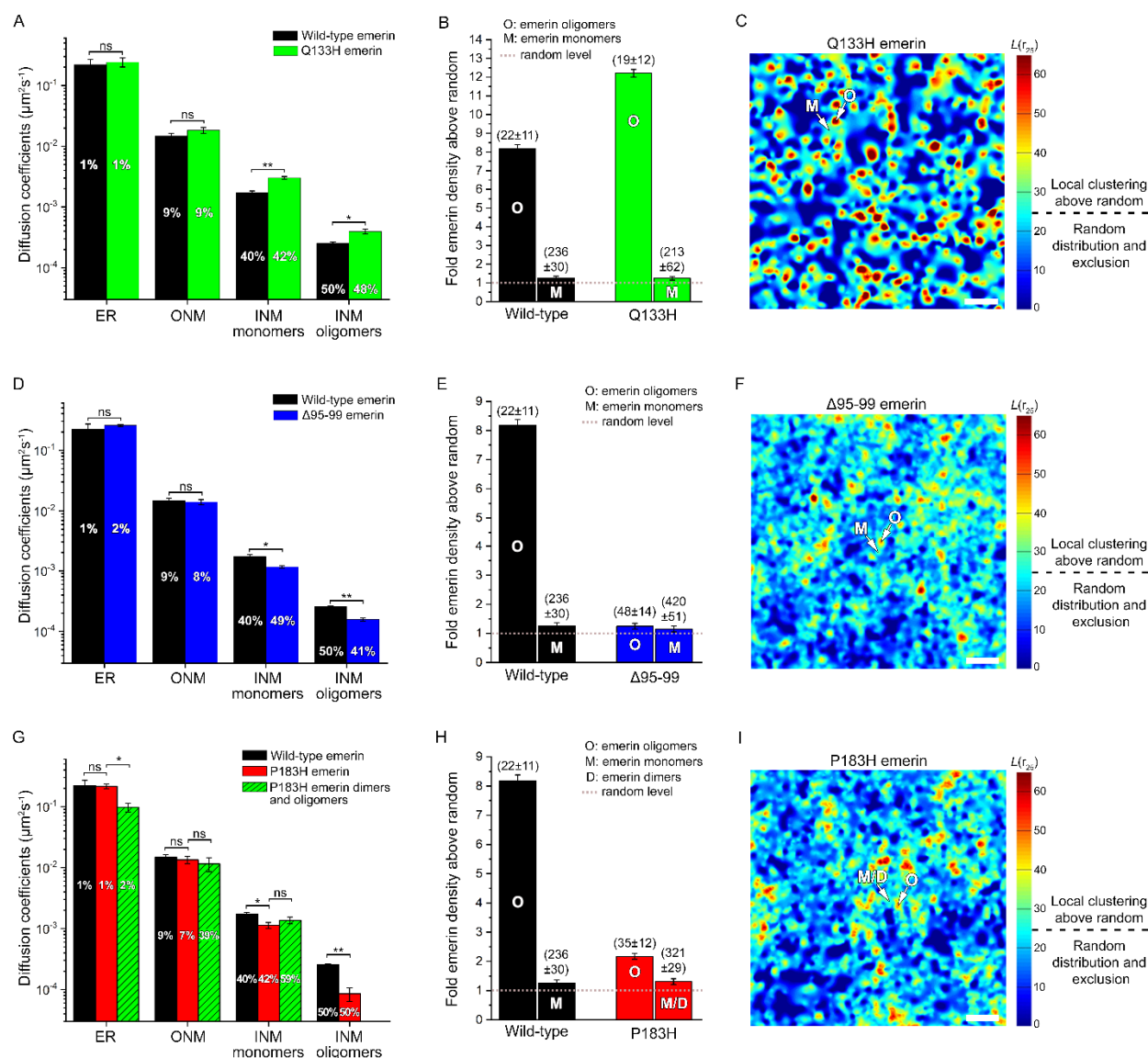
Fig. 6. Emerin mutants exhibit modified lateral mobilities and defective oligomerization. (A) Diffusion coefficients (±s.e.m.) and percentages of wild-type and Q133H emerin. (B) Molecular densities above random (±s.e.m.) for wild-type and Q133H emerin oligomers (O) and monomers (M). (C) Local cluster map of Q133H emerin. M: monomer areas, O: oligomer nanodomains. Scale: 250 nm. (D) Diffusion coefficients (±s.e.m.) and percentages of wild-type and Δ95-99 emerin. (E) Molecular densities above random (±s.e.m.) for Δ95-99 (208092 localizations, 8 nuclei) and wild-type emerin oligomers (O) and monomers (M). (F) Local cluster map of Δ95-99 emerin. Scale: 250 nm. (G) Diffusion coefficients (±s.e.m.) and percentages of wild-type and P183H emerin compared to complemented P183H emerin-GFP-emerin species. (H) Molecular densities above random (±s.e.m.) for P183H and wild-type emerin oligomers (O) and monomers/dimers (M/D). (I) Local cluster map of P183H emerin. M/D: monomer/dimer areas, O: oligomer nanodomains. Scale: 250 nm. For (A, D and G), t-test, ns: non-significant, *: $p<0.05$, **: $p<0.01$. For (B, E and H), values in parenthesis represent the size (±s.e.m.) of each domain in nanometers.

39

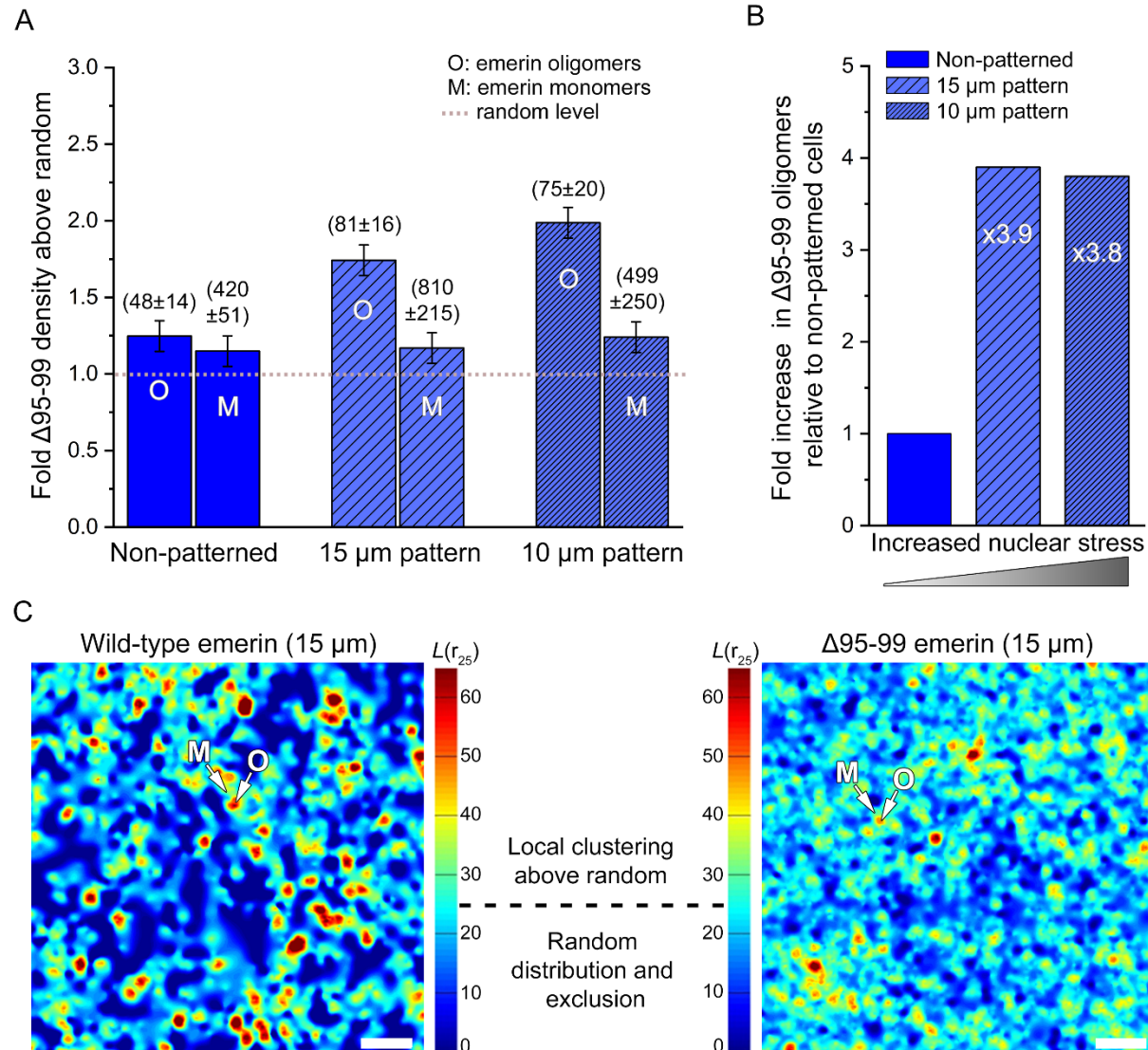1100
1101

Fig. 7. **Insufficient oligomerization of Δ95-99 emerin mutant against mechanical stress.** (A) Molecular densities above random (±s.e.m.) for Δ95-99 emerin oligomers (O) and monomers (M) in non-patterned cells or after nuclear deformation on 15 and 10 µm micropatterns. Values in parenthesis represent the size (±s.e.m.) of each domain in nanometers. (B) Changes in Δ95-99 emerin oligomers as a function of nuclear stress on 15 and 10 µm micropatterns. (C) Local cluster maps of wild-type and Δ95-99 emerin after nuclear deformation on 15 µm micropatterns. M: monomer areas, O: oligomer nanodomains. Scale: 250 nm.
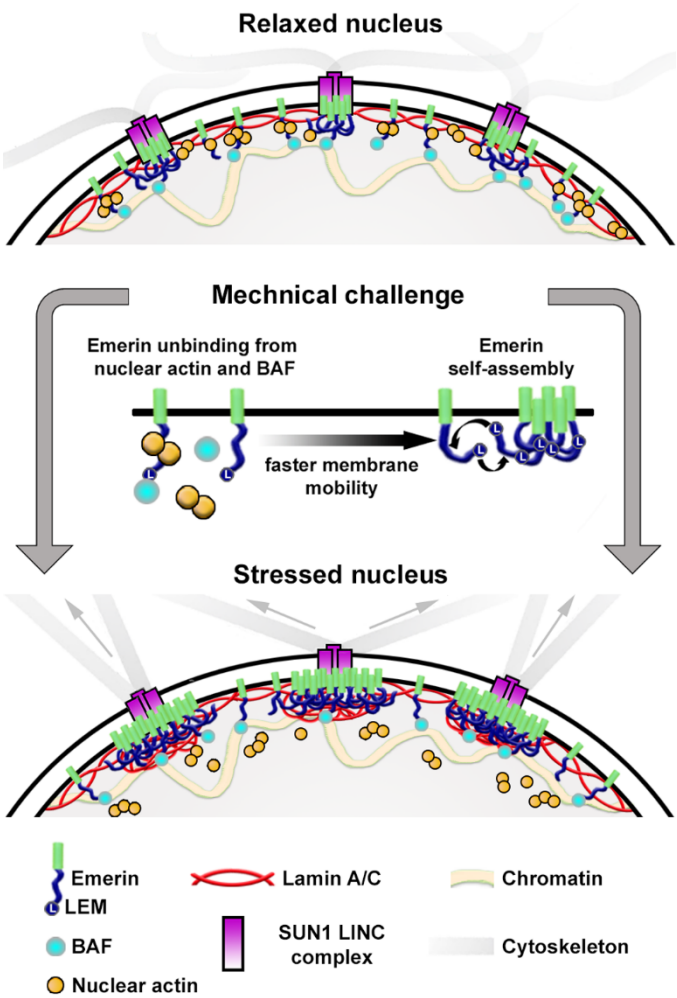
1102
1103
1104
1105
1106
1107
1108
1109
1110
1111

1112

1113

1114 **Fig. 8**. **Model of emerin re-organization at the nuclear envelope in response to mechanical**
1115 **challenges.** Emerin monomer unbinding from nuclear actin and BAF induces increased lateral
1116 mobility at the inner nuclear membrane and favors LEM domain interactions with binding sites
1117 along the intrinsically disordered region of other emerin, for the controlled formation of emerin
1118 oligomers at SUN1 LINC complexes and their stabilization by lamin A/C.
1119

References

Arsenovic, P. T., Ramachandran, I., Bathula, K., Zhu, R., Narang, J. D., Noll, N. A., Lemmon, C. A., Gundersen, G. G. and Conway, D. E. (2016). Nesprin-2G, a Component of the Nuclear LINC Complex, Is Subject to Myosin-Dependent Tension. *Biophys J* **110**, 34-43.

Baarlink, C., Plessner, M., Sherrard, A., Morita, K., Misu, S., Virant, D., Kleinschnitz, E. M., Harniman, R., Alibhai, D., Baumeister, S. et al. (2017). A transient pool of nuclear F-actin at mitotic exit controls chromatin organization. *Nature Cell Biology* **19**, 1389-1399.

Bautista, M., Fernandez, A. and Pinaud, F. (2019). A Micropatterning Strategy to Study Nuclear Mechanotransduction in Cells. *Micromachines (Basel)* **10**.

Belin, B. J., Cimini, B. A., Blackburn, E. H. and Mullins, R. D. (2013). Visualization of actin filaments and monomers in somatic cell nuclei. *Molecular Biology of the Cell* **24**, 982-94.

Bengtsson, L. and Wilson, K. L. (2004). Multiple and surprising new functions for emerin, a nuclear membrane protein. *Current Opinion in Cell Biology* **16**, 73-9.

Berk, J. M., Maitra, S., Dawdy, A. W., Shabanowitz, J., Hunt, D. F. and Wilson, K. L. (2013a). O-Linked beta-N-acetylglucosamine (O-GlcNAc) regulates emerin binding to barrier to autointegration factor (BAF) in a chromatin- and lamin B-enriched "niche". *Journal of Biological Chemistry* **288**, 30192-209.

Berk, J. M., Simon, D. N., Jenkins-Houk, C. R., Westerbeck, J. W., Gronning-Wang, L. M., Carlson, C. R. and Wilson, K. L. (2014). The molecular basis of emerin-emerin and emerin-BAF interactions. *Journal of Cell Science* **127**, 3956-69.

Berk, J. M., Tifft, K. E. and Wilson, K. L. (2013b). The nuclear envelope LEM-domain protein emerin. *Nucleus* **4**, 298-314.

Burger, M., Schmitt-Koopmann, C. and Leroux, J.-C. (2020). DNA unchained: two assays to discover and study inhibitors of the DNA clustering function of barrier-to-autointegration factor. *Scientific Reports* **10**, 12301.

Clements, L., Manilal, S., Love, D. R. and Morris, G. E. (2000). Direct interaction between emerin and lamin A. *Biochemical and Biophysical Research Communications* **267**, 709-14.

Crisp, M., Liu, Q., Roux, K., Rattner, J. B., Shanahan, C., Burke, B., Stahl, P. D. and Hodzic, D. (2006). Coupling of the nucleus and cytoplasm: role of the LINC complex. *Journal of Cell Biology* **172**, 41-53.

Cui, Y., Hameed, F. M., Yang, B., Lee, K., Pan, C. Q., Park, S. and Sheetz, M. (2015). Cyclic stretching of soft substrates induces spreading and growth. *Nature Communications* **6**, 6333.

Demmerle, J., Koch, A. J. and Holaska, J. M. (2012). The nuclear envelope protein emerin binds directly to histone deacetylase 3 (HDAC3) and activates HDAC3 activity. *The Journal of Biological Chemistry* **287**, 22080-8.

Dopie, J., Skarp, K. P., Rajakyla, E. K., Tanhuanpaa, K. and Vartiainen, M. K. (2012). Active maintenance of nuclear actin by importin 9 supports transcription. *Proceedings of the National Academy of Sciences of the United States of America* **109**, E544-52.

Emery, A. E. and Dreifuss, F. E. (1966). Unusual type of benign x-linked muscular dystrophy. *J Neurol Neurosurg Psychiatry* **29**, 338-42.

Fairley, E. A., Kendrick-Jones, J. and Ellis, J. A. (1999). The Emery-Dreifuss muscular dystrophy phenotype arises from aberrant targeting and binding of emerin at the inner nuclear membrane. *Journal of Cell Science* **112 (Pt 15)**, 2571-82.

Fernandez, A., Bautista, M., Stanciauskas, R., Chung, T. and Pinaud, F. (2017). Cell-Shaping Micropatterns for Quantitative Super-Resolution Microscopy Imaging of Membrane Mechanosensing Proteins. *ACS Applied Materials & Interfaces* **9**, 27575-27586.

Fidzianska, A. and Hausmanowa-Petrusewicz, I. (2003). Architectural abnormalities in muscle nuclei. Ultrastructural differences between X-linked and autosomal dominant forms of EDMD. *Journal of the Neurological Sciences* **210**, 47-51.

Frock, R. L., Kudlow, B. A., Evans, A. M., Jameson, S. A., Hauschka, S. D. and Kennedy, B. K. (2006). Lamin A/C and emerin are critical for skeletal muscle satellite cell differentiation. *Genes Dev* **20**, 486-500.

Getis, A. and Franklin, J. (1987). Second-Order Neighborhood Analysis of Mapped Point Patterns. *Ecology* **68**, 473-477.

Guilluy, C., Osborne, L. D., Van Landeghem, L., Sharek, L., Superfine, R., Garcia-Mata, R. and Burridge, K. (2014). Isolated nuclei adapt to force and reveal a mechanotransduction pathway in the nucleus. *Nature Cell Biology* **16**, 376-81.

Haque, F., Lloyd, D. J., Smallwood, D. T., Dent, C. L., Shanahan, C. M., Fry, A. M., Trembath, R. C. and Shackleton, S. (2006). SUN1 interacts with nuclear lamin A and cytoplasmic nesprins to provide a physical connection between the nuclear lamina and the cytoskeleton. *Mol Cell Biol* **26**, 3738-51.

Haque, F., Mazzeo, D., Patel, J. T., Smallwood, D. T., Ellis, J. A., Shanahan, C. M. and Shackleton, S. (2010). Mammalian SUN protein interaction networks at the inner nuclear membrane and their role in laminopathy disease processes. *Journal of Biological Chemistry* **285**, 3487-98.

Haraguchi, T., Kojidani, T., Koujin, T., Shimi, T., Osakada, H., Mori, C., Yamamoto, A. and Hiraoka, Y. (2008). Live cell imaging and electron microscopy reveal dynamic processes of BAF-directed nuclear envelope assembly. *Journal of Cell Science* **121**, 2540-54.

Hennen, J., Saunders, C. A., Mueller, J. D. and Luxton, G. W. G. (2018). Fluorescence fluctuation spectroscopy reveals differential SUN protein oligomerization in living cells. *Molecular Biology of the Cell* **29**, 1003-1011.

Herrada, I., Samson, C., Velours, C., Renault, L., Ostlund, C., Chervy, P., Puchkov, D., Worman, H. J., Buendia, B. and Zinn-Justin, S. (2015). Muscular Dystrophy Mutations Impair the Nuclear Envelope Emerin Self-assembly Properties. *ACS Chemical Biology* **10**, 2733-42.

Hirano, Y., Segawa, M., Ouchi, F. S., Yamakawa, Y., Furukawa, K., Takeyasu, K. and Horigome, T. (2005). Dissociation of Emerin from Barrier-to-autointegration Factor Is Regulated through Mitotic Phosphorylation of Emerin in a Xenopus Egg Cell-free System*. *Journal of Biological Chemistry* **280**, 39925-39933.

Ho, C. Y., Jaalouk, D. E., Vartiainen, M. K. and Lammerding, J. (2013). Lamin A/C and emerin regulate MKL1–SRF activity by modulating actin dynamics. *Nature* **497**, 507-511.

Holaska, J. M., Kowalski, A. K. and Wilson, K. L. (2004). Emerin caps the pointed end of actin filaments: evidence for an actin cortical network at the nuclear inner membrane. *PLoS Biology* **2**, E231.

1205   **Holt, I., Clements, L., Manilal, S. and Morris, G. E.** (2001). How does a g993t mutation in
1206   the emerin gene cause Emery-Dreifuss muscular dystrophy? *Biochemical and Biophysical*
1207   *Research Communications* **287**, 1129-33.

1208   **Jahed, Z., Fadavi, D., Vu, U. T., Asgari, E., Luxton, G. W. G. and Mofrad, M. R. K.**
1209   (2018). Molecular Insights into the Mechanisms of SUN1 Oligomerization in the Nuclear
1210   Envelope. *Biophysical Journal* **114**, 1190-1203.

1211   **Kirby, T. J. and Lammerding, J.** (2018). Emerging views of the nucleus as a cellular
1212   mechanosensor. *Nature Cell Biology* **20**, 373-381.

1213   **Lagardère, M., Chamma, I., Bouilhol, E., Nikolski, M. and Thoumine, O.** (2020). FluoSim:
1214   simulator of single molecule dynamics for fluorescence live-cell and super-resolution imaging
1215   of membrane proteins. *Scientific Reports* **10**, 19954.

1216   **Lammerding, J., Hsiao, J., Schulze, P. C., Kozlov, S., Stewart, C. L. and Lee, R. T.** (2005).
1217   Abnormal nuclear shape and impaired mechanotransduction in emerin-deficient cells. *Journal*
1218   *of Cell Biology* **170**, 781-91.

1219   **Lee, K. K., Haraguchi, T., Lee, R. S., Koujin, T., Hiraoka, Y. and Wilson, K. L.** (2001).
1220   Distinct functional domains in emerin bind lamin A and DNA-bridging protein BAF. *Journal*
1221   *of Cell Science* **114**, 4567-73.

1222   **Loi, M., Cenni, V., Duchi, S., Squarzoni, S., Lopez-Otin, C., Foisner, R., Lattanzi, G. and**
1223   **Capanni, C.** (2016). Barrier-to-autointegration factor (BAF) involvement in prelamin A-
1224   related chromatin organization changes. *Oncotarget* **7**, 15662-77.

1225   **Lombardi, M. L., Jaalouk, D. E., Shanahan, C. M., Burke, B., Roux, K. J. and**
1226   **Lammerding, J.** (2011). The interaction between nesprins and sun proteins at the nuclear
1227   envelope is critical for force transmission between the nucleus and cytoskeleton. *Journal of*
1228   *Biological Chemistry* **286**, 26743-53.

1229   **Lu, W., Gotzmann, J., Sironi, L., Jaeger, V. M., Schneider, M., Lüke, Y., Uhlén, M.,**
1230   **Szigyarto, C. A., Brachner, A., Ellenberg, J. et al.** (2008). Sun1 forms immobile
1231   macromolecular assemblies at the nuclear envelope. *Biochim Biophys Acta* **1783**, 2415-26.

1232   **Maurer, M. and Lammerding, J.** (2019). The Driving Force: Nuclear Mechanotransduction
1233   in Cellular Function, Fate, and Disease. *Annual Review of Biomedical Engineering* **21**, 443-
1234   468.

1235   **Mislow, J. M. K., Holaska, J. M., Kim, M. S., Lee, K. K., Segura-Totten, M., Wilson, K.**
1236   **L. and McNally, E. M.** (2002). Nesprin-1α self-associates and binds directly to emerin and
1237   lamin A in vitro. *FEBS Letters* **525**, 135-140.

1238   **Mortensen, K. I., Churchman, L. S., Spudich, J. A. and Flyvbjerg, H.** (2010). Optimized
1239   localization analysis for single-molecule tracking and super-resolution microscopy. *Nature*
1240   *Methods* **7**, 377-81.

1241   **Ostlund, C., Ellenberg, J., Hallberg, E., Lippincott-Schwartz, J. and Worman, H. J.**
1242   (1999). Intracellular trafficking of emerin, the Emery-Dreifuss muscular dystrophy protein.
1243   *Journal of Cell Science* **112 (Pt 11)**, 1709-19.

1244   **Ostlund, C., Sullivan, T., Stewart, C. L. and Worman, H. J.** (2006). Dependence of
1245   diffusional mobility of integral inner nuclear membrane proteins on A-type lamins.
1246   *Biochemistry* **45**, 1374-82.

1247 **Pengo, T., Holden, S. J. and Manley, S.** (2015). PALMsiever: a tool to turn raw data into
1248 results for single-molecule localization microscopy. *Bioinformatics* **31**, 797-8.

1249 **Perry, G. L. W.** (2004). SpPack: spatial point pattern analysis in Excel using Visual Basic for
1250 Applications (VBA). *Environmental Modelling & Software* **19**, 559-569.

1251 **Phair, R. D., Gorski, S. A. and Misteli, T.** (2004). Measurement of dynamic protein binding
1252 to chromatin in vivo, using photobleaching microscopy. *Methods in Enzymology* **375**, 393-414.

1253 **Pinaud, F. and Dahan, M.** (2011). Targeting and imaging single biomolecules in living cells
1254 by complementation-activated light microscopy with split-fluorescent proteins. *Proceedings of*
1255 *the National Academy of Sciences* **108**, E201-E210.

1256 **Roberts, R. C., Sutherland-Smith, A. J., Wheeler, M. A., Jensen, O. N., Emerson, L. J.,**
1257 **Spiliotis, II, Tate, C. G., Kendrick-Jones, J. and Ellis, J. A.** (2006). The Emery-Dreifuss
1258 muscular dystrophy associated-protein emerin is phosphorylated on serine 49 by protein kinase
1259 A. *FEBS Journal* **273**, 4562-75.

1260 **Rowat, A. C., Lammerding, J. and Ipsen, J. H.** (2006). Mechanical properties of the cell
1261 nucleus and the effect of emerin deficiency. *Biophysical Journal* **91**, 4649-64.

1262 **Sakaki, M., Koike, H., Takahashi, N., Sasagawa, N., Tomioka, S., Arahata, K. and**
1263 **Ishiura, S.** (2001). Interaction between emerin and nuclear lamins. *Journal of Biochemistry*
1264 **129**, 321-7.

1265 **Salpingidou, G., Smertenko, A., Hausmanowa-Petrucewicz, I., Hussey, P. J. and**
1266 **Hutchison, C. J.** (2007). A novel role for the nuclear membrane protein emerin in association
1267 of the centrosome to the outer nuclear membrane. *Journal of Cell Biology* **178**, 897-904.

1268 **Samson, C., Celli, F., Hendriks, K., Zinke, M., Essawy, N., Herrada, I., Arteni, A. A.,**
1269 **Theillet, F. X., Alpha-Bazin, B., Armengaud, J. et al.** (2017). Emerin self-assembly
1270 mechanism: role of the LEM domain. *FEBS Journal* **284**, 338-352.

1271 **Samson, C., Petitalot, A., Celli, F., Herrada, I., Ropars, V., Le Du, M. H., Nhiri, N.,**
1272 **Jacquet, E., Arteni, A. A., Buendia, B. et al.** (2018). Structural analysis of the ternary
1273 complex between lamin A/C, BAF and emerin identifies an interface disrupted in autosomal
1274 recessive progeroid diseases. *Nucleic Acids Research* **46**, 10460-10473.

1275 **Samwer, M., Schneider, M. W. G., Hoefler, R., Schmalhorst, P. S., Jude, J. G., Zuber, J.**
1276 **and Gerlich, D. W.** (2017). DNA Cross-Bridging Shapes a Single Nucleus from a Set of
1277 Mitotic Chromosomes. *Cell* **170**, 956-972 e23.

1278 **Schneider, C. A., Rasband, W. S. and Eliceiri, K. W.** (2012). NIH Image to ImageJ: 25
1279 years of image analysis. *Nature Methods* **9**, 671-5.

1280 **Schutz, G. J., Schindler, H. and Schmidt, T.** (1997). Single-molecule microscopy on model
1281 membranes reveals anomalous diffusion. *Biophysical Journal* **73**, 1073-80.

1282 **Sengupta, P., Jovanovic-Talisman, T., Skoko, D., Renz, M., Veatch, S. L. and Lippincott-**
1283 **Schwartz, J.** (2011). Probing protein heterogeneity in the plasma membrane using PALM and
1284 pair correlation analysis. *Nature Methods* **8**, 969-75.

1285 **Serge, A., Bertaux, N., Rigneault, H. and Marguet, D.** (2008). Dynamic multiple-target
1286 tracing to probe spatiotemporal cartography of cell membranes. *Nature Methods* **5**, 687-94.

1287 **Shimi, T., Koujin, T., Segura-Totten, M., Wilson, K. L., Haraguchi, T. and Hiraoka, Y.**
1288 (2004). Dynamic interaction between BAF and emerin revealed by FRAP, FLIP, and FRET
1289 analyses in living HeLa cells. *Journal of Structural Biology* **147**, 31-41.

45

Soumpasis, D. M. (1983). Theoretical analysis of fluorescence photobleaching recovery experiments. *Biophysical Journal* **41**, 95-7.

Stephens, A. D., Banigan, E. J., Adam, S. A., Goldman, R. D. and Marko, J. F. (2017). Chromatin and lamin A determine two different mechanical response regimes of the cell nucleus. *Molecular Biology of the Cell* **28**, 1984-1996.

Stoynova, L., Solórzano, R. and Collins, E. D. (2004). Generation of large deletion mutants from plasmid DNA. *BioTechniques* **36**, 402-4, 406.

Subach, F. V., Patterson, G. H., Renz, M., Lippincott-Schwartz, J. and Verkhusha, V. V. (2010). Bright monomeric photoactivatable red fluorescent protein for two-color super-resolution sptPALM of live cells. *Journal of the American Chemical Society* **132**, 6481-91.

Talamas, J. A. and Hetzer, M. W. (2011). POM121 and Sun1 play a role in early steps of interphase NPC assembly. *Journal of Cell Biology* **194**, 27-37.

Talkop, U. A., Talvik, I., Sõnajalg, M., Sibul, H., Kolk, A., Piirsoo, A., Warzok, R., Wulff, K., Wehnert, M. S. and Talvik, T. (2002). Early onset of cardiomyopathy in two brothers with X-linked Emery-Dreifuss muscular dystrophy. *Neuromuscular Disorders* **12**, 878-81.

Thompson, R. E., Larson, D. R. and Webb, W. W. (2002). Precise nanometer localization analysis for individual fluorescent probes. *Biophysical Journal* **82**, 2775-83.

Tifft, K. E., Bradbury, K. A. and Wilson, K. L. (2009). Tyrosine phosphorylation of nuclear-membrane protein emerin by Src, Abl and other kinases. *Journal of Cell Science* **122**, 3780-90.

Tokunaga, M., Imamoto, N. and Sakata-Sogawa, K. (2008). Highly inclined thin illumination enables clear single-molecule imaging in cells. *Nature Methods* **5**, 159-61.

van de Linde, S., Löschberger, A., Klein, T., Heidbreder, M., Wolter, S., Heilemann, M. and Sauer, M. (2011). Direct stochastic optical reconstruction microscopy with standard fluorescent probes. *Nature Protocols* **6**, 991-1009.

Wolter, S., Loschberger, A., Holm, T., Aufmkolk, S., Dabauvalle, M. C., van de Linde, S. and Sauer, M. (2012). rapidSTORM: accurate, fast open-source software for localization microscopy. *Nature Methods* **9**, 1040-1.